Acta Biomaterialia 169 (2023) 66–87

Contents lists available at ScienceDirect

Acta Biomaterialia

journal homepage: www.elsevier.com/locate/actbio

Review article

An atlas of the heterogeneous viscoelastic brain with local power-law attenuation synthesised using Prony-series

Oisín Morrison, Michel Destrade, Bharat B. Tripathi*

School of Mathematical and Statistical Sciences, University of Galway, University Road, Galway, Ireland

ARTICLE INFO

Article history:
Received 4 April 2023
Revised 16 July 2023
Accepted 24 July 2023
Available online 27 July 2023

Keywords:
Brain matter
Heterogeneity
Brain viscoelasticity
Brain wave physics
Finite element head models
Relaxation mechanisms
Power-law attenuation
Dispersion relations
Prony-series

ABSTRACT

This review addresses the acute need to acknowledge the mechanical heterogeneity of brain matter and to accurately calibrate its local viscoelastic material properties accordingly. Specifically, it is important to compile the existing and disparate literature on attenuation power-laws and dispersion to make progress in wave physics of brain matter, a field of research that has the potential to explain the mechanisms at play in diffuse axonal injury and mild traumatic brain injury in general. Currently, viscous effects in the brain are modelled using Prony-series, i.e., a sum of decaying exponentials at different relaxation times. Here we collect and synthesise the Prony-series coefficients appearing in the literature for twelve regions: brainstem, basal ganglia, cerebellum, corona radiata, corpus callosum, cortex, dentate gyrus, hippocampus, thalamus, grey matter, white matter, homogeneous brain, and for eight different mammals: pig, rat, human, mouse, cow, sheep, monkey and dog. Using this data, we compute the fractional-exponent attenuation power-laws for different tissues of the brain, the corresponding dispersion laws resulting from causality, and the averaged Prony-series coefficients.

Statement of significance

Traumatic brain injuries are considered a silent epidemic and finite element methods (FEMs) are used in modelling brain deformation, requiring access to viscoelastic properties of brain. To the best of our knowledge, this work presents 1) the first multi-frequency viscoelastic atlas of the heterogeneous brain, 2) the first review focusing on viscoelastic modelling in both FEMs and experimental works, 3) the first attempt to conglomerate the disparate existing literature on the viscoelastic modelling of the brain and 4) the largest collection of viscoelastic parameters for the brain (212 different Prony-series spanning 12 different tissues and 8 different animal surrogates). Furthermore, this work presents the first brain atlas of attenuation power-laws essential for modelling shear waves in brain.

Glossary

We adopt the following conventions in this paper:

- We reserve line markers for different categories as shown in Fig. 1 throughout the paper.
- Owing to space limitations, it was not always possible to have legends given on all subplots. In such cases, the legends on any of the subplots apply for all other subplots in the figure.
- Unless otherwise stated, when error regions are shown in figures, they correspond to the region spanned by one standard deviation errors of the parameters.

1. Introduction

According to the World Health Organisation, neurological disorders are one of the greatest threats to public health, with traumatic brain injury (TBI) being the leading cause of death and disability in children and young adults around the world [1]. The problem is growing, and it is expensive as well as life-threatening. In the Republic of Ireland alone, a small country of five million inhabitants, about 350 million euros were spent on TBIs in 2010, out of nearly 6 billion euros spent in total on brain disorders [2]. It is thus of

* Corresponding author.
E-mail address: bharat.tripathi@universityofgalway.ie (B.B. Tripathi).

https://doi.org/10.1016/j.actbio.2023.07.040

Fig. 1. Legends used for different animals. FE refers to data from finite element models.

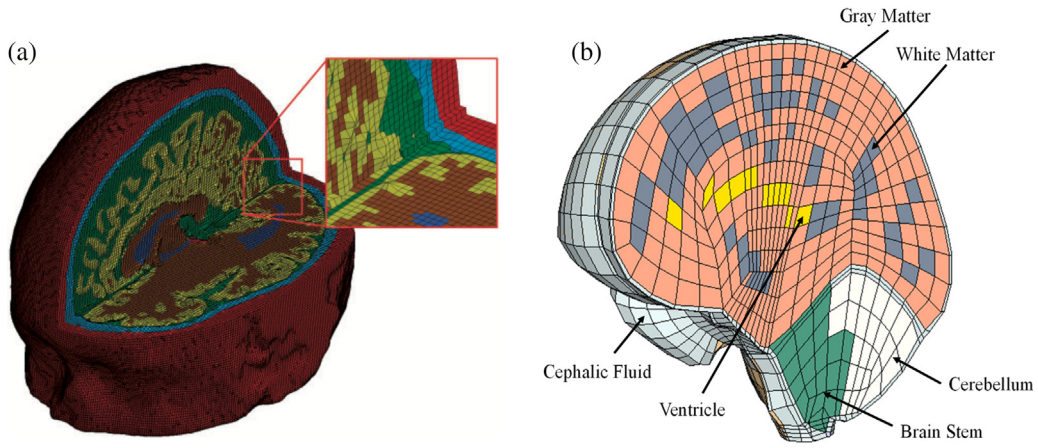

Fig. 2. Two recent FE head models, incorporating differing elastic properties for different areas of the brain, but the same (homogeneous) viscoelastic data everywhere. (a): The finite element mesh of the high fidelity 3D model from Imperial College London [8]. Colour coding is: skin (red), skull (light blue), cerebrospinal fluid (green), grey matter (yellow), white matter (brown) and ventricles (dark blue). (b): The UCD Head Trauma model, originally designed by Horgan and Gilchrist [9] (picture taken from Cinelli et al. [10]). Note that its most recent version does include viscous heterogeneity [11]. (For interpretation of the references to colour in this figure legend, the reader is referred to the web version of this article.)

critical importance that a better understanding of TBI is achieved to help combat this issue.

Most clinical indicators used for predicting TBI, typically linear and/or rotational accelerations, are global and not appropriate to evaluate regional brain strains and strain rates. But these local deformations and motions play an important role in the development of mild TBI events, such as concussion in contact sports or repetitive impacts over a lifetime [3]. Hence there is a pressing need for accurate material parameters that can be used in detailed finite element (FE) computer simulations [4,5] (see Fig. 2 for two recent models).

However, there is an enormous amount of variation in the viscoelastic parameters used by existing FE models, due to dated experimental sources, differing testing protocols, temperature, type of tissue, type of animal, post-mortem times, tissue preservation modes, and many other factors. The brain is also often considered as a homogeneous tissue from the point of view of viscoelastic properties, while it has been experimentally observed to be heterogeneous in that respect [6]. The disparity in experimental data and the assumption of homogeneity are problematic when it comes to studying mild TBI, because they lead to very different predictions when the same event is simulated, as shown by Zhao et al. [7] (see Fig. 3).

Recently shear shock waves were generated and observed experimentally in the brain, and proposed as a possible explanation for diffuse axonal injury [12,13], a major type of TBI. Furthermore, in direct impact injuries, it has been observed that injuries can occur far from the point of impact [14]. The reason for this distant effect has not yet been established, but the formation of shear shock waves has been hypothesised to be a possible mechanism. Theoretically, cubic non-linearity must be invoked to model these nonlinear shear waves [15]; it follows that they generate mostly odd harmonics [16], and very high local accelerations [17]. Importantly, these high local accelerations are not generated instantly and instead are a result of cumulative nonlinear effect. The maximum acceleration is reached after a few centimetres of propagation in brain, before dissipating. Recent studies in 2D head phantoms have furthermore shown that this mechanism can predict peak accelerations far from the point of impact [17,18]. This is thus a promising and important hypothesis to test because it could have major repercussions for the prediction and understanding of TBIs, the design of helmets and other protective headgear, and the suitability of existing FE models for modelling TBI. In this work, we are only confined to shear deformation similar to those resulting from direct impact injuries. They result in shear shock waves unlike the compressional shock waves in blast-TBIs which could have frequency range of kHz to MHz. These two effects happen at different scales as there is three orders of magnitude difference between the shear modulus and the bulk modulus. Importantly, a biofidelic modelling of the wave physics involved in shear shock wave for-

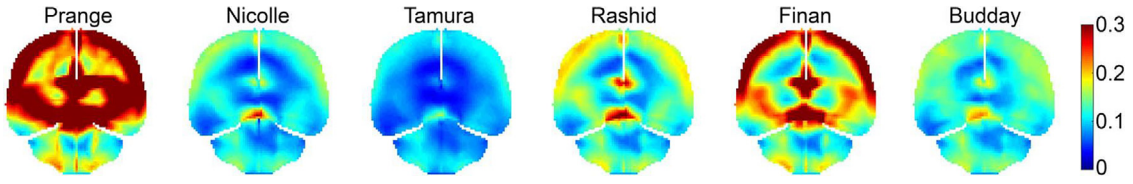

Fig. 3. When the same FE model is used to simulate the same high-velocity impact, but with different material parameters from the experimental literature, it yields very different predictions of the cumulative maximum principal strains generated [7]. Here the experimental data is taken (left to right) from Refs. [19–24].

mation and propagation requires accurate experimental data for the heterogeneous material properties of the brain – specifically, attenuation power-laws and dispersion relations.

To the best of our knowledge, there exists only one map detailing the viscoelastic properties of the heterogeneous brain, namely the recent paper by Hiscox et al. [25]. In that work, the authors collect storage and loss moduli data using a shear wave at the given frequency of 50 Hz and magnetic resonance elastography (MRE) imaging. They give this data for subcortical grey matter structures, white matter tracts, and regions of the cerebral cortex.

In this paper, we go a step further by providing viscoelastic data, used in FE models and recent experimental data, valid for multiple frequency ranges and for twelve key regions of the brain: brainstem, basal ganglia, cerebellum, corona radiata, corpus callosum, cortex, dentate gyrus, hippocampus, thalamus, grey matter, white matter, and homogeneous brain. We also provide viscoelastic data also for eight different animals: pig, rat, human, mouse, cow, sheep, monkey and dog. We conglomerate multiple Prony-series data, the most common implementation of viscoelastic effects used in current state-of-the-art FE models. From this data, we synthesise average attenuation power-laws, dispersion relations and also Prony-series.

2. Theoretical background

Soft solids like tissues are often modelled using hyperelastic models capable of describing large strain nonlinear deformations. At the same time, tissues are often highly attenuating and dispersing, i.e., the excitation amplitude decays with time and distance, and different frequencies travel at different speeds. Conventionally these effects are modelled using the linear [26] and quasi-linear [27] viscoelastic theories.

2.1. Linear viscoelasticity

In linear viscoelasticity, the stress response to a constant strain decreases with time, a feature which is referred to as the stress relaxation of the material. This is modelled using the fading memory or hereditary integral:

$$\sigma(t) = \int_{-\infty}^{t} m(t-\tau)\epsilon(\tau)d\tau := m(t) * \epsilon(t), \tag{1}$$

where $\sigma(t)$ is the stress (in Pa), $\epsilon(t)$ is the strain (dimensionless), and $m(t-\tau)$ is the instantaneous stress-response function to an impulse in strain $\epsilon(\tau)$ imposed at time τ for the time interval $t-\tau$. This is the so-called convolution operation, denoted by "$*$". In the frequency space, this hereditary integral can be written as

$$\sigma(\omega) = M(\omega)\epsilon(\omega), \tag{2}$$

where $M(\omega)$ is the *dynamic modulus*, corresponding to the impulse response of the material.

However, in solid mechanics, the step-response is often more relevant than the instantaneous response. The memory integral can be rewritten as:

$$\sigma(t) = \int_{-\infty}^{t} g(t-\tau)\frac{\partial\epsilon(\tau)}{\partial\tau}d\tau = g(t) * \frac{\partial\epsilon(t)}{\partial t} = \frac{\partial g(t)}{\partial t} * \epsilon(t), \tag{3}$$

where $g(t)$ is the stress response to unit-step strain, often called the *relaxation function*. The last equality in the above equation is due to the commutative property of the convolution integral. Also, Eqs. (1) and (3) give the connection

$$m(t) = \frac{\partial g(t)}{\partial t}, \tag{4}$$

or in frequency space

$$M(\omega) = i\omega G(\omega), \tag{5}$$

leading to

$$\sigma(\omega) = M(\omega)\epsilon(\omega) = i\omega G(\omega)\epsilon(\omega), \tag{6}$$

where $G(\omega)$ is the complex *relaxation modulus*.

Conventionally, the relaxation functions presented in the TBI literature are approximated using a *Prony-series* of decreasing exponentials,

$$g(t) = M_\infty + \sum_{j=1}^{N} M_j \exp(-t/\tau_j), \tag{7}$$

where $\tau_j = \eta_j/M_j$ $(j = 1, \ldots, N)$ corresponds to the j^{th} Maxwell element, which is a Hookean element with elastic modulus M_j placed in series with a Newtonian element with coefficient of viscosity η_j.

Note that $g(0) = M_\infty + \sum_{j=1}^{N} M_j =: M_0$, which defines the latter quantity. Then a dimensionless Prony-series $\hat{g}(t)$ with $\hat{g}(0) = 1$ can be defined as

$$\hat{g}(t) = \hat{M}_\infty + \sum_{j=1}^{N} \hat{M}_j \exp(-t/\tau_j), \tag{8}$$

where $\hat{M}_j = M_j/M_0$.

In frequency space, the corresponding dynamic modulus, $M(\omega)$, or relaxation modulus, $G(\omega)$, can be written as

$$M(\omega) = i\omega G(\omega) = M_\infty + \sum_{j=1}^{N} M_j \frac{i\omega\tau_j}{1+i\omega\tau_j}. \tag{9}$$

Using this complex modulus, the attenuation in soft solids can be quantified using the *quality factor* $Q(\omega)$ defined as [28]

$$Q(\omega) = \frac{\mathrm{Re}\{\mathrm{M}(\omega)\}}{\mathrm{Im}\{\mathrm{M}(\omega)\}} = \frac{M'(\omega)}{M''(\omega)}, \tag{10}$$

where $M'(\omega) = \mathrm{Re}\{M(\omega)\}$ and $M''(\omega) = \mathrm{Im}\{M(\omega)\}$ are the *storage modulus* and the *loss modulus*, respectively, given explicitly by

$$M'(\omega) = \mathrm{Re}\{M(\omega)\} = M_\infty + \sum_{j=1}^{N} M_j \frac{\omega^2\tau_j^2}{1+\omega^2\tau_j^2}, \tag{11}$$

$$M''(\omega) = \mathrm{Im}\{M(\omega)\} = \sum_{j=1}^{N} M_j \frac{\omega\tau_j}{1+\omega^2\tau_j^2}. \tag{12}$$

Note that whilst these equations can be evaluated for any value of ω, it is not physically meaningful to evaluate them over all frequencies as the Prony-series are fitted over a finite time interval. Specifically, it is valid to evaluate these functions at the (angular) frequencies $\omega = \beta_j$, $j = 1, \ldots, N$, where $\beta_j = 1/\tau_j$. A suitable frequency range can thus be computed from the Prony-series coefficients as $[\min_j \beta_j, \max_j \beta_j]$. In the case of a one-term Prony-series, this would give a single point and thus then the extended frequency range $[0.1\beta_1, 10\beta_1]$ is used (see Nicolle et al. [20,29]). This is also consistent with conventions of the commercial finite element solver Abaqus [30].

The other physical behaviour associated with the attenuation is dispersion due to causality [31]. Consider the linear shear wave equation in an elastic media,

$$\frac{\partial^2 u}{\partial t^2} = \frac{1}{\rho}\frac{\partial\sigma}{\partial x} = \frac{\mu}{\rho}\frac{\partial^2 u}{\partial x^2} = c^2\frac{\partial^2 u}{\partial x^2}, \tag{13}$$

where ρ is the mass density, μ is the shear modulus, and $c = \sqrt{\mu/\rho}$ is the shear wave speed. On substituting the harmonic solution

$$u = \exp[i(\omega t - kx)], \tag{14}$$

where u is the particle displacement, ω is the angular frequency, and k is the wavenumber, we find the following connection for the phase velocity c,

$$c = \omega/k. \tag{15}$$

Now consider the viscoelastic case as in [32], where

$$\sigma = m(t) * \epsilon = m(t) * \frac{\partial u}{\partial x}, \tag{16}$$

so that the wave equation reads

$$\rho \frac{\partial^2 u}{\partial t^2} = m(t) * \frac{\partial^2 u}{\partial x^2}. \tag{17}$$

Taking the Fourier transform $\mathcal{F}$ with respect to time of the above equation gives

$$(i\omega)^2 \mathcal{F}\{u\} = \frac{M(\omega)}{\rho} \frac{\partial^2}{\partial x^2} \mathcal{F}\{u\}. \tag{18}$$

To calculate the right-hand side of the above equation, let us rewrite Eq. (14) as

$$u(x,t) = \exp(i\omega t) \exp(-iK(\omega)x), \tag{19}$$

where $K(\omega)$ is the complex wavenumber in the viscoelastic media. Then Eq. (18) gives

$$\frac{K(\omega)}{\omega} = \sqrt{\frac{\rho}{M(\omega)}}. \tag{20}$$

Equation (14) can be rewritten using $K(\omega) = K'(\omega) + iK''(\omega)$ as

$$u = \exp\{K''(\omega)x\} \exp\{i(\omega t - K'(\omega)x)\}, \tag{21}$$

showing that the (real) phase velocity c is given by

$$\frac{1}{c(\omega)} = \frac{K'(\omega)}{\omega} = \mathrm{Re}\left\{\sqrt{\frac{\rho}{M(\omega)}}\right\}. \tag{22}$$

Note $c(\omega)$ is not a Fourier transform, it is just a function in frequency space. Equation (22) furthermore yields two solutions but only the principal solution is valid (the other yields $c(\omega) < 0$), which is unphysical).

The two quantities $Q(\omega)$ and $c(\omega)$ are then used to compute the *attenuation* $\alpha(\omega)$ via the relation [32,33]:

$$Q(\omega) = \frac{1}{2}\left[\frac{\omega}{c(\omega)\alpha(\omega)} - \frac{c(\omega)\alpha(\omega)}{\omega}\right]. \tag{23}$$

On solving this quadratic equation in $\alpha(\omega)$ we get

$$\alpha(\omega) = \frac{-Q + \sqrt{Q^2+1}}{c(\omega)/\omega}, \tag{24}$$

while ignoring the non-physical solution where $\alpha(\omega) < 0$.

Alternatively, the attenuation of transient waves like ultrasound/shear wave in soft solids is commonly characterized using a *fractional-exponent power-law*,

$$\alpha(\omega) = a\omega^b = \alpha_0 f^b, \tag{25}$$

where a, b and α_0 are constants. Alternatively, in log-log space, $\ln\alpha$ follows an empirical linear law: $\ln\alpha = \ln a + b \ln\omega$.

2.2. Quasi-linear viscoelasticity

For large amplitude deformations, assuming a linear behaviour is no longer valid as the stress and strain exhibit a nonlinear relationship of relaxation. Fung [27] proposed the concept of *quasi-linear viscoelasticity* (QLV), with the assumption of multiplicative decomposition of the stress into a dimensionless relaxation function of time $\hat{g}(t)$ with $\hat{g}(0) = 1$ and the instantaneous elastic stress $d\sigma_e(t)/dt$. On applying the superposition principle, we get

$$\sigma(t) = \int_0^t \hat{g}(t-\tau)\frac{d\sigma_e(\tau)}{d\tau}d\tau = \int_0^t \frac{d\hat{g}(t-\tau)}{d\tau}$$
$$\sigma_e(\tau)d\tau = \int_0^t \hat{m}(t-\tau)\sigma_e(\tau)d\tau. \tag{26}$$

The QLV formulation therefore ends up using the entire mathematical formulation of linear viscoelastic theory as described in the previous section. We can then relate $g(t)$ and $\hat{g}(t)$, as:

$$g(t) = M_0\hat{g}(t) = M_\infty + \sum_{j=1}^{N} M_j e^{-t/\tau_j}, \tag{27}$$

where M_0 is the instantaneous shear modulus of the hyperelastic strain energy density. Table 1 gives the expressions for M_0 of some commonly used hyperelastic models.

These two viscous modelling approaches are the two most common approaches used for describing viscoelastic effects. Another approach is the fractional viscoelastic model [34], which is still not fully adopted due to its mathematical complexities.

2.3. Calculating Prony-series from attenuation power-laws

It is possible to compute averaged attenuation power-laws from the data, but many current models are heavily reliant on the use of Prony-series. As a result, it is important to provide a means of determining averaged Prony-series from an attenuation power-law $\alpha(\omega) = a\omega^b$, valid over an angular frequency range $[\omega_1, \omega_2]$.

Firstly, the dispersion can be calculated for $\omega \in [\omega_1, \omega_2]$ via the Kramers-Kronig relation [31]:

$$\frac{1}{c(\omega)} - \frac{1}{c(\omega_0)} = \begin{cases} a\tan\left(\frac{b\pi}{2}\right)(\omega^{b-1} - \omega_0^{b-1}); & \text{when } b \in (0,2)\backslash\{1\} \\ -\frac{2}{\pi}a\omega_0^b(\ln\omega - \ln\omega_0); & b = 1 \end{cases}. \tag{28}$$

Note that this calculation requires a reference value $c(\omega_0)$. Furthermore, we note that the case $b = 1$ will not occur for our fitted parameters.

Ergo, using Eq. (28) and Eq. (23), one can directly compute the inverse quality factor. Recall that the inverse of the quality factor is also directly obtainable from a Prony-series via Eq. (10), and note that the value of M_0 does not influence the quality factor. This means that a dimensionless Prony-series with parameters $\hat{M}_j = \frac{M_j}{M_0}$ can also be used. It is thus possible to write directly:

$$Q^{-1}(\omega) = \frac{1}{2}\left[\frac{\omega}{a\omega^b c(\omega_0)}\left(ac(\omega_0)\tan\left(\frac{b\pi}{2}\right)(\omega^{b-1} - \omega_0^{b-1}) + 1\right) - \frac{a\omega^b c(\omega_0)}{\omega}\left(ac(\omega_0)\tan\left(\frac{b\pi}{2}\right)(\omega^{b-1} - \omega_0^{b-1}) + 1\right)^{-1}\right]^{-1}$$
$$= \frac{\sum_{j=1}^{N}\hat{M}_j\frac{\omega\tau_j}{1+\omega^2\tau_j^2}}{\hat{M}_\infty + \sum_{j=1}^{N}\hat{M}_j\frac{\omega^2\tau_j^2}{1+\omega^2\tau_j^2}}. \tag{29}$$

Thus, together with the additional constraint that $\hat{M}_\infty + \sum_{j=1}^{N}\hat{M}_j = 1$, it is possible to directly curve fit the N-term Prony-series once given N. As per Abaqus recommendations, the order of the Prony-series should not be larger than the number of logarithmic decades spanned by the test data [30]. Thus, this furthermore sets N as

$$N = \left\lfloor \log_{10}\left(\frac{\omega_2}{\omega_1}\right)\right\rfloor. \tag{30}$$

Table 1
Instantaneous shear moduli of common hyperelastic strain-energy densities.

Hyperelastic Model	W	M_0
Neo-Hookean	$\frac{1}{2}\mu(I_1-3)$	μ
Mooney-Rivlin	$C_1(I_1-3)+C_2(I_2-3)$	$2(C_1+C_2)$
2-term Polynomial[a]	$C_{10}(I_1-3)+C_{01}(I_2-3)+C_{20}(I_1-3)^2+C_{02}(I_2-3)^2$	$2(C_{10}+C_{01})$
Ogden	$\sum_{n=1}^{N}\frac{\mu_n}{\alpha_n}\left(\lambda_1^{\alpha_n}+\lambda_2^{\alpha_n}+\lambda_3^{\alpha_n}-3\right)$	$\frac{1}{2}\sum_{n=1}^{N}\mu_n\alpha_n$
Gasser-Ogden-Holzapfel[b]	$\frac{1}{2}\mu(I_1-3)+\frac{k_1}{2k_2}\left[e^{k_2(I_1-3)^2}-1\right]$	μ

[a] Without cross term $C_{11}(I_1-3)(I_2-3)$.
[b] In the isotropic case.

Lastly, it remains to compute the value of M_0, which is done via the formula [33]

$$M_0 = \rho c(\omega_0)^2 \frac{|\hat{M}(\omega_0)| + \mathrm{Re}\{\hat{M}(\omega_0)\}}{2|\hat{M}(\omega_0)|^2}, \tag{31}$$

where $\hat{M}(\omega)$ refers to the dynamic modulus derived using the dimensionless Prony-series.

3. Methods

We summarise the data collected in our literature review, and we provide details on our approach for calculating averaged attenuation power-laws and Prony-series.

3.1. Summary of literature review

We collected a total of 181 differing Prony-series from 48 different experimental papers, spanning twelve regions of interest and eight different animal types (see supplementary materials). The cortex was the most measured region in the dataset, with 43 Prony-series. The other tissues had fewer data: brainstem (23), corona radiata (19), homogeneous brain (19), cerebellum (18), hippocampus (18), corpus callosum (17), thalamus (11), dentate gyrus (7) and basal ganglia (6). To investigate the effect of surrogate tissues, we also collected the species used in the experiments. The most commonly used animal surrogate was porcine tissue, with 56 Prony-series. A total of eight different surrogates were used in our collected experimental data - namely, rat (52), human (45), mouse (13), cow (12), sheep (1), monkey (1), and dog (1).

We only collected recent experimental data (from the past 25 years), from a variety of experimental protocols, including indentation tests, shear tests, tensile tests and compression tests. All of these protocols were testing ex-vivo brain tissue. In-vivo testing is possible by MRE, but there are some limitations and assumptions associated with current methods [35–37]. Indeed, large discrepancies between various MRE measurements exist, sometimes by an order of magnitude [35]. There are also discrepancies between the results of mechanical tests and elastography results, such as for uniaxial compression [38]. Budday et al. [39] noted this discrepancy for experiments into age-dependence for brain tissue. There are also issues with reconstruction methodologies for MRE [40,41]. Consequently, we did not collect MRE experimental results here, to remove this source of additional variation.

Data was collected regardless of differences in experimental protocols, species, sex, temperature, or other factors, although factors such as choice of surrogate tissue and brain region were recorded. It is well known that several other factors such as age [37,42], sex [43,44], animal [45,46], experimental protocol [47,48], temperature [49–51], preservation [52], humidity [53] and post-mortem time [54,55] can affect experimental results. There are already studies comparing results obtained from similar experimental procedures [6,56]. However, in this review we focus on comparing the data used in FE modelling, where data is generally used from a wide range of experiments irrespective of the experimental conditions and protocols. Furthermore, Chatelin et al. [47] found in their review that the disparity in results was independent of experimental protocol.

In relation to Prony-series used in FE models, we found a total of 31 unique Prony-series. A total of 23 different FE models were considered in this work. In alphabetical order, they are the following: ADAPT [57], ANISO KTH v1 [58], ANISO KTH v2 [59], ATLAS [60], Cai et al. (CAI) [61], Chen et al. (CHEN) [62], ICM [8], Khanuja & Unni (KHANUJA) [63], KTH v2 [64], SIMON v0 [65], SIMON v1 [66], Subramaniam et al. (SUBRAM) [67], Tse et al. (TSE) [68], UCD v1 [9], UCD v2 [11], WSUBIM [69], Yang et al. (YANG) [70], ULP v0 [71], ULP v1 [72,73], WHIM v1 [74], WHIM v2 [75,76], Yang et al. (YANG) [70] and YEAHM [77,78] models. The most commonly modelled tissue is the homogeneous brain, with 12 different Prony-series. Most data consist of only one-term Prony-series. The same problems with variations due to differing experimental protocols also apply to these datasets. Furthermore, there are also multiple instances of differing Prony-series being derived from the same experimental sources due to differences in fitting methods. In some cases, even the order of the Prony-series can change between studies - for example, from the data of Shuck and Advani [79], the WHIM v2 model obtains a 2-term Prony-series [75,76], whilst the models of Yang et al. [70], Tse et al. [68], Chen et al. [62] and ULP v0 [71] have a one-term Prony-series.

We also note that FE models are not always using experimental results directly. FE models such as ATLAS [60] have opted to use optimisation schemes based on running many simulations and picking parameters which best reproduce experimentally determined histories. This approach is problematic because the parameter optimisation results now depend upon intrinsic properties of the model such as the geometry. This means that even while using the exact same validations, different models can yield substantially different predictions [80]. Models furthermore do not always use the same types of validations, which can also lead to varying predictions [81].

Another common practice in FE models is to model the hyperelastic and viscoelastic response separately. These effects can be either additively decomposed using the theory of linear viscoelasticity (Section 2.1) or multiplicatively decomposed using the theory of quasi-linear viscoelasticity (Section 2.2). Some groups also merge together different experimental data: they source viscoelastic properties and hyperelastic properties from different experiments (possibly using different experimental protocols) and combine them together. However, one can obtain different fits for each hyperelastic model; this can be seen in the work of MacManus et al. [82] and Eskandari et al. [83]. Furthermore, using different hyperelastic models essentially amounts to altering the value of M_0. Scaling viscoelastic experimental data is frequently implemented in FE models e.g. the KTH model [84] simply scales the data by a factor of 2, and the ULP v1 [73] model scales the data using the results of the 1977 paper of Khalil et al. [85]. However, this scaling affects both the attenuation and dispersion laws, thus changing the mechanical behaviour of the tissue compared to that of the original experimental paper. Nevertheless, in order to compare FE models

Table 2
Sources of experimental viscoelastic data (in chronological order) used by 19 current state-of-the-art FE models for the obtention of *dimensionless* Prony-series $\hat{g}(t)$.

Reference	Year	Species	FE Model(s)
MacManus et al. [86]	2017	Rat	UCD v2 [11]
Miller et al. [60][b]	2016	-	ATLAS [60]
Rashid et al. [87]	2012	Pig	Khanuja-Unni [63], YEAHM [77,78]
Kleiven [84] (using data from Nicolle et al. [29])	2005	Pig	ADAPT [57], ICM [8], KTH v2 [64]
Cloots et al. [88] (using data from Nicolle et al. [29])	2005	Pig	ANISO-KTH v1 [58], ANISO-KTH v2 [59], WHIM v1 [74]
Zhang et al. [89][a]	2004	-	Chen & Ostoja-Starzewski [62]
Willinger & Baumgartner [72][a]	2003	-	ULP v1 [72,73]
Takhounts et al. [90]	2003	Human	Cai et al. [61], SIMon v1 [66]
Zhang et al. [69][b]	2001	-	Tse et al. [68], UCD v2 [11], WSUBIM [69], Yang et al. [70]
Willinger et al. [71] (using data from Shuck & Advani [79])	1972	Human	Tse et al. [68], ULP v0 [71], Yang et al. [70]
Zhang et al. [91] (using data from Shuck & Advani [79])	1972	Human	Tse et al. [68], Yang et al. [70]
Zhao & Ji [76] (using data from Shuck & Advani [79])	1972	Human	WHIM v2 [75,76]
Mendis et al. [92] (using data from Estes & McElhaney [93])	1970	Human	Subramaniam et al. [67], UCD v1 [9]

[a] No experimental viscoelastic source was found.
[b] These papers use optimised parameters selected to match experiment results and thus thus do not come directly from experimental viscoelastic data. For example, Zhang et al. [91] used datasets such as pressure data by Troseille et al. [94] and Nahum et al. [95] for optimisation.

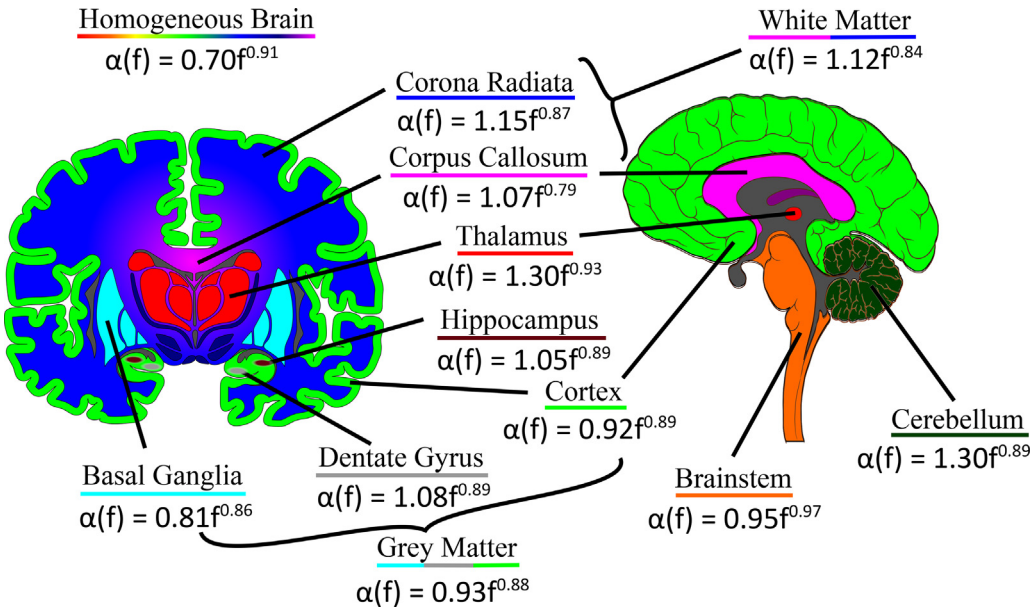

Fig. 4. Schematic of brain sections coronal (left) and sagittal (right) with twelve different attenuation power-laws with nine different regions (basal ganglia, brainstem, corona radiata, corpus callosum, cortex, dentate gyrus, hippocampus, and thalamus) and the remaining three summarising the white matter, grey matter and the homogeneous brain.

with the experimental literature, we use predictions from all such Prony-series, regardless if they have been scaled or have multiple experimental sources.

We performed a thorough literature review of experimental papers and of computational simulation papers, with a total of more than 100 research articles. Most of the finite element method (FEM) based numerical solvers use viscoelastic material properties from the thirteen papers presented in Table 2. Many of the FEM solvers currently assume that brain is a homogeneous material, and only implement a single-term Prony-series, mostly with the assumption of linear viscoelasticity. Some recent FEM implementations use the QLV implementation. We gathered the viscoelastic properties, specifically, the Prony-series parameters implemented in the FEM solvers as well as those recorded in the experimental papers for different tissue types, namely: 1) homogeneous brain, 2) brainstem, 3) basal ganglia, 4) cerebellum, 5) corona radiata, 6) corpus callosum, 7) cortex, 8) dentate gyrus, 9) hippocampus, 10) thalamus, 11) grey matter and 12) white matter. These regions are depicted in Fig. 4. A total of 8 different animals were considered: pig, rat, human, mouse, cow, sheep, monkey and dog. In the main article, we provide a detailed analysis of the viscoelastic behaviour of the homogeneous brain as used in FEM solvers, and relegate the viscoelastic properties of other tissue types to the supplementary material.

Some models include anisotropy [58,59,75,76,96,97] or porosity [53,98] in addition to linear or quasi-linear viscoelasticity, but we did not report these effects (in general, fibre reinforcement does not contribute significantly to the mechanical response in the parallel or perpendicular shearing directions [96]). Similarly, we ignored compressibility because brain matter is near incompressible [99]. Furthermore, experimental papers oftentimes provided multiple Prony-series fits for the same region, but with differing strain rates [100–102], strains [103–105], indentation depths [106], loading rates [48], impact angle [107], velocity [107], loading modes (e.g. tension, compression, shear etc.) [24], direction relative to fibres [97,108], loading cycle [109], boundary condition [110], preconditioning or no preconditioning [24,48,106], injured or uninjured tissue [106], plane of experiment [86,108,111], and animal age [86,112–115]. Having many Prony-series come from a given study was not desirable because that study would disproportionally affect the final averaged results and because it is well known from previous literature reviews that viscoelastic parameters may vary

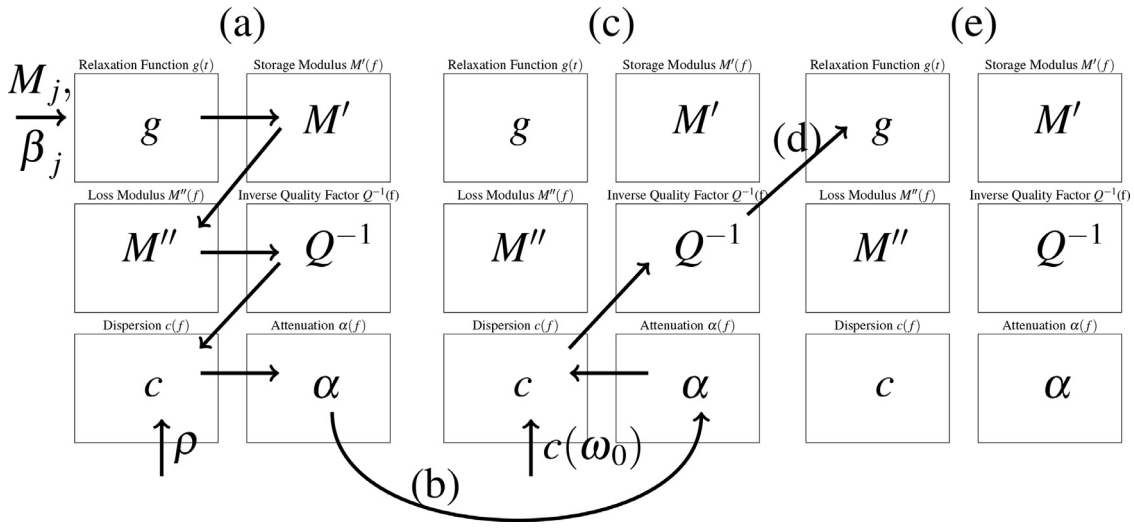

Fig. 5. The workflow process consists of five steps: (a) forward calculation, (b) average power-law calculation, (c) backward calculation, (d) averaged Prony-series fitting and (e) re-calculation.

immensely from one study to another [39,47,56]. As a result, we decided to take fits from mature and uninjured tissue only. When choice was available, we took fits for the highest strain rate, strain, indentation depth and velocity. When available, we took data for all modes, the first loading cycles, and no slip boundary conditions. Fits in directions orthogonal fibres were also preferred, to neglect anisotropic effects. Data from the axial plane was preferred because slices are more homogeneous along this plane; if that data was unavailable, then the sagittal plane was taken instead. Finally, if neither of these were available, the coronal plane was taken. Impact angles of 0 degrees were also preferred. Lastly, preconditioned fits were taken when available, as they were observed to be closer to the other data, and also some unconditioned fits were found to have $M_\infty = 0$ [106], which is unphysical as it corresponds to a fluid. Cases where different Prony-series were provided for different locations within the same region were kept, and highest order Prony-series were taken in all cases. When differing fits were provided for different animals [86,90,116], these were also kept.

For Prony-series fits used in FE models, we found that only a single FE model provided specific viscoelastic parameters for the corpus callosum [61]. This fit was thus considered as white matter owing to a lack of other data. Similarly, only one FE model provided viscoelastic properties for the cerebrum [68], so this was included within the homogeneous brain data for FE models.

Following the literature review, we focused on a total of six key quantities: the relaxation function $g(t)$, storage modulus $M'(\omega)$, loss modulus $M''(\omega)$, inverse quality factor $Q^{-1}(\omega)$, dispersion $c(\omega)$ and attenuation $\alpha(\omega)$. We adopted a workflow consisting of five key steps to analyse the different viscoelastic parameters extracted from the literature, see summary in Fig. 5. The steps are as follows.

3.2. Forward calculation

- The coefficients of the Prony-series, M_j and $\beta_j = 1/\tau_j$, $j = 1, \ldots, N$, are recorded for each study during the literature review. These values together can be used to create the relaxation function $g(t)$ using Eq. (7), or alternatively to calculate the dimensionless parameters $\hat{M}_j$ along with the instantaneous shear modulus M_0 via Eq. (8).
- The Prony-series data is then used to calculate the storage modulus $M'(\omega)$ via Eq. (11) and the loss modulus $M''(\omega)$ via Eq. (12).
- With the help of the loss and storage moduli, the inverse quality factor $Q^{-1}(\omega)$ is calculated using Eq. (10) along with the dispersion relation $c(\omega)$ via Eq. (22). A mass density $\rho = 1000$ kg/m^3 was used for all tissues.
- Using the quality factor and the dispersion, the attenuation power-law $\alpha(\omega)$ is calculated from Eq. (23).

3.3. Average power-law calculation

Now attenuations are calculated for each of the Prony-series. It is then possible to synthesise an averaged attenuation power-law from these calculated curves. Specifically, we conduct a linear fit in the log-log space using the $\alpha(\omega)$ laws evaluated only at the frequencies corresponding to their Prony-series decay coefficients $\omega = \beta_j$, $j = 1, \ldots, N$. The valid frequency range of a fit was then taken to be $[\min_j \beta_j, \max_j \beta_j]$. Fits were only undertaken if there were at least three datapoints.

3.4. Backward calculation

Following the average power-law calculation, we obtain an averaged power-law $\ln \alpha(\omega) = \ln a + b \ln \omega$, along with standard deviations $\sigma_{\ln a}$ and σ_b. Using a reference value of $c = 2.1$ m/s at a frequency of 75 Hz derived from experiments on homogeneous brain tissue [12,17], it is possible to calculate the dispersion from the Kramers-Kronig relation as defined in Eq. (28). The quality factor can then subsequently be calculated using the derived attenuation and dispersion laws via Eq. (23). To determine the errors in the predicted quality, we calculate its minimum and maximum using the parameter choices $\ln a \pm \sigma_{\ln a}$ and $b \pm \sigma_b$, respectively. A single error metric can be computed as the mean of the errors in the lower and upper bounds.

3.5. Averaged Prony-series fitting

The backward calculation yields quality factors valid over a range of angular frequencies $[\omega_1, \omega_2]$. From this data, it is then possible to directly perform a curve fitting exercise for the dimensionless Prony-series parameters as per Eq. (29). The order of the Prony-series is set by Eq. (30). Here, we evaluated the inverse quality at 1000 equally spaced points on log-scale, which we call logarithmically spaced points in the valid interval $[\omega_1, \omega_2]$. Each of these points also has an associated error. Curve fitting for

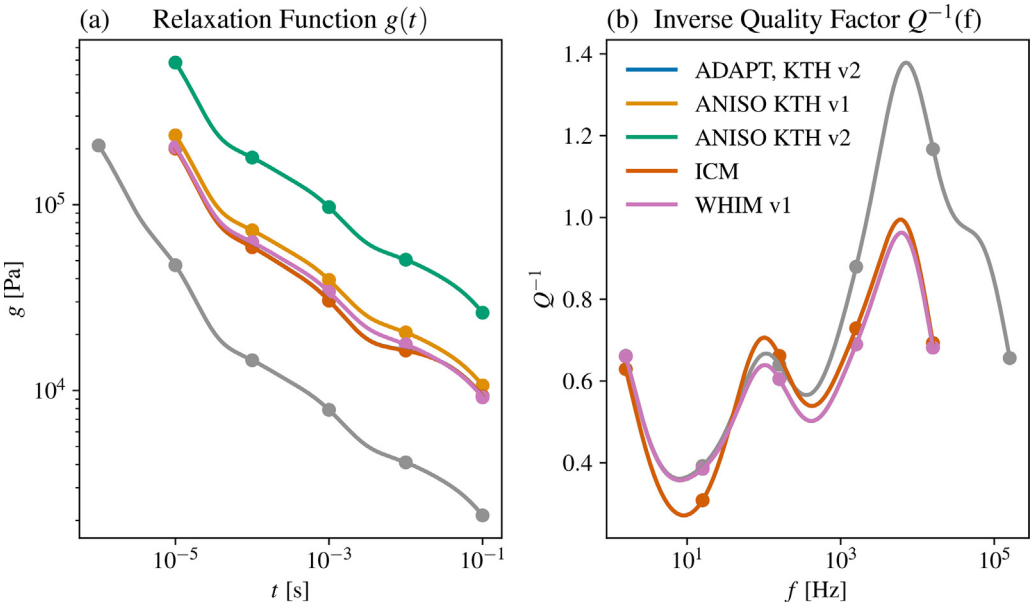

Fig. 6. Anomalous Prony-series predictions (grey) and their corrected versions (coloured) for (a) the relaxation function and (b) inverse quality factor.

Eq. (29) given these values and errors was performed using the "trust region reflective" algorithm, based on the work of Branch et al. [117] and implemented in Scipy [118]. This algorithm allows one to give lower and upper bounds for the required parameters, based on physical intuition. For example, we know the parameters M_j should be constrained on $[0, 1]$. To ensure that the parameters β_j are physically relevant, we can partition the interval $[\omega_{\min}, \omega_{\max}]$ into $n+1$ logarithmically equidistant intervals and use these as the bounded regions. Once the dimensionless parameters were fitted, we calculated the instantaneous shear modulus M_0 using Eq. (31). Again, we used the references values $\rho = 1000$ kg/m^3 and $c = 2.1$ m/s at 75 Hz. Then the fitted Prony-series is entirely defined. Lastly, we also provide the attenuation power-laws used, so that users can conduct their own Prony-series fits if desired.

4. Results and discussion

4.1. Anomalies in Prony-series

In some cases, Prony-series predictions were not in line with the general data. Specifically, a number of Prony-series were found to predict an inverse quality factor greater than 1. This has problematic physical implications - a dissipation factor greater than 1 would correspond to the case where more energy is dissipated than the total energy of the wave [119]. As a result, corrections to these series were required in order to make them comparable to the general data. To this end, the dimensionless series was truncated by entirely removing the highest frequency term in the series. All other terms in the series were left unchanged. The quality was then found to be strictly below 1 for the range of valid frequencies as desired. However, conducting such a truncation necessarily alters either M_0, or of M_∞. A choice thus must be made on which quantity to keep constant. In this work, M_0 was kept constant since this is a more robust experimental quantity than M_∞. That is, it is physically impossible to measure M_∞ as this would require waiting for an infinite amount of time. Thus, instead in experiments a large time is used to approximate the value at $t \to \infty$. However, this cut-off time is arbitrary which this means that values of M_∞ can vary. Furthermore, we found that the keeping M_0 constant yielded results more in line with our general findings.

Figure 6 shows the original Prony-series (in grey color) and the truncated series (in color). These Prony-series are primarily derived from Nicolle's work [20] and have been used by the ANISO KTH models and its variants, Imperial College, and Worchester models. As evident from the right-subplot, the unphysical case of $Q^{-1} \geq 1$ is present for high frequencies. On the other hand, the truncated Prony-series indeed produce $Q^{-1} < 1$. However, this truncation does overestimate $g(t)$ with respect to the original series. Nevertheless, the truncated Prony-series produce results consistent with the average results.

Prony-series differing substantially from the rest of the literature were also not included in this review, such as the curve of Mendizabal et al. [120]. Since these are outliers, it was necessary to disregard them in order not to skew results.

4.2. Attenuation power-laws in homogeneous brain

To understand the currently used approaches in FE models, we discuss the predictions of viscoelastic FE data for the homogeneous brain.

Most of the computational models still use the homogeneous assumption while describing the viscoelastic properties of the brain matter. In this section, we consider the different Prony-series used in the common FE models describing the homogeneous brain deformation.

The Prony-series collected were fitted using Eq. (7) which gives a continuous function as shown in Fig. 7a. Most of the relaxation functions are close to each other except the ones from Tse et al. [68] and ULP v0 [71] (light-blue), which uses the experimental data from Shuck and Advani [79].

There is significant variation in the Prony-series data, which is unsurprising given the experimental sources summarised in Table 2, many of which are 50 years old. This reliance on dated experimental data is problematic because experimental protocols have changed greatly over the past 50 years thanks to new experimental data and approaches [56]. Studies indicating temperature and post-mortem time effects have lead to newer experimental approaches with better controls. For example, the data from the work of Shuck and Advani in 1972 [79] is an outlier, overestimating both the storage and loss moduli as compared to other studies [47,56]. This data was obtained hours after autopsy, which itself may have

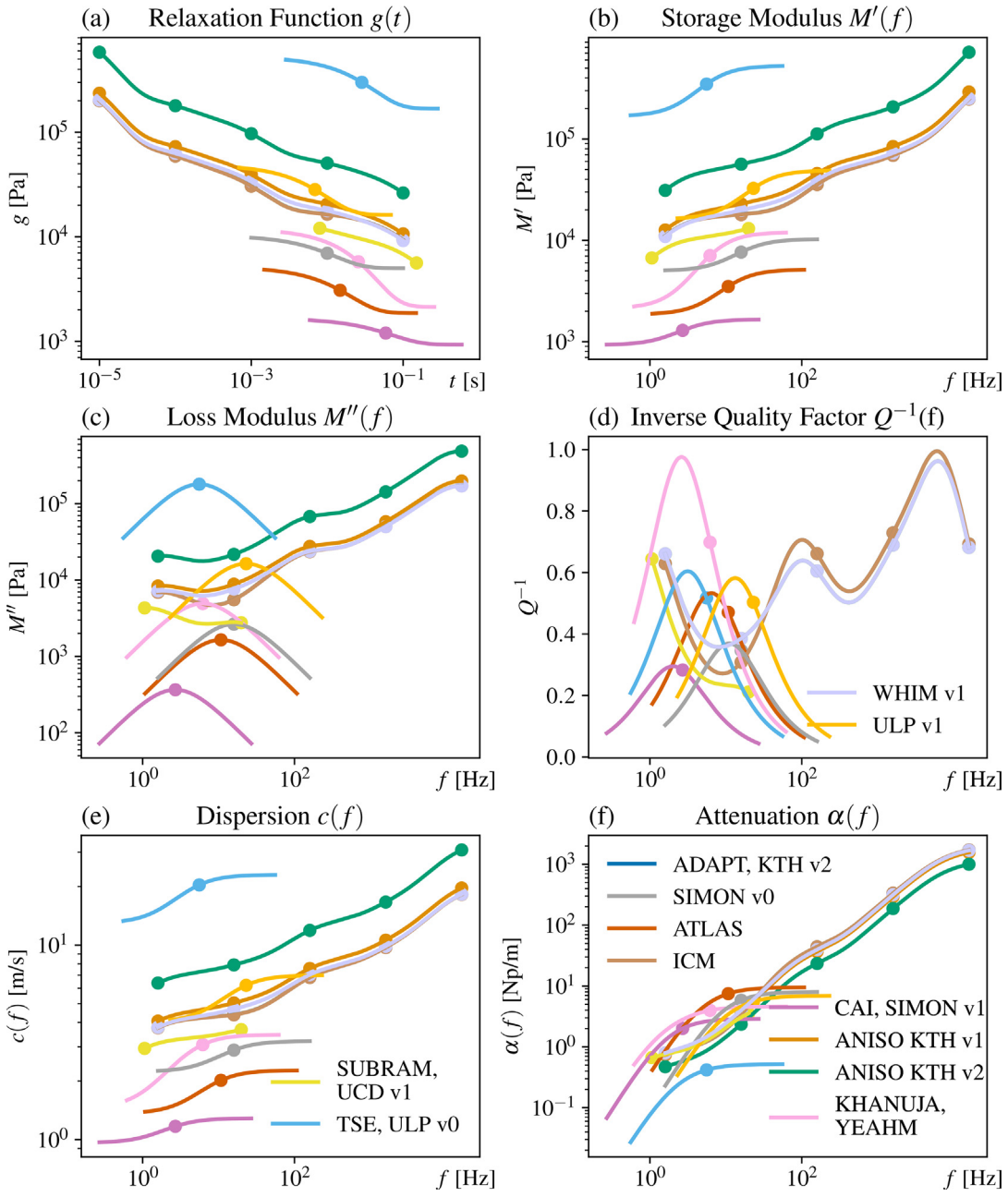

Fig. 7. Derivation of attenuation and dispersion laws from each of the Prony-series used in FE models. Shown are the predictions for (a) the relaxation function, (b) storage modulus, (c) loss modulus, (d) inverse quality factor, (e) dispersion and finally (f) attenuation.

been hours or days post-mortem. This issue is particularly problematic as it is well known that brain tissue stiffness increases quickly with post-mortem time. Weickenmeier et al. [54] found that within 16 h post-mortem, the loss and storage moduli were twice as stiff.

Notwithstanding these extra considerations, there are large variations in the experimental protocol used in experiments in general [56], which makes it difficult to get consistency between results. However, as seen in Table 2, these older papers are some of the few experimental studies on human brain that are being used in FE models. The experimental data used by the UCD v2 [11] model from MacManus et al. [86] are obtained from experiments on rats, which is not ideal because the structure of the rodent brain is considerably different to that of a human [114]. Dai et al. [46] recommend instead the use of experimental data from large animals (e.g. pig, rabbit, sheep, etc.) above rodents when data from human brains are not available, and Nicolle et al. [20] report no significant difference in viscoelastic behaviour between porcine and human brain matter.

Furthermore, the assumption that the brain is homogeneous with respect to viscoelastic properties is weak, as results can vary greatly depending on what region of the brain is being considered [86]. It is thus important that the data for the homogeneous brain be taken from a representative region. However, the data of Nicolle et al. [29] and of Shuck & Advani [79] are in fact obtained from the corona radiata region. This is a white matter region which is mechanically quite different from the mixed white-grey matter region studied by Rashid et al. [121].

Predicted quantities from the collected Prony-series for the homogeneous brain as used in FE models are shown in Fig. 7. In gen-

eral, most Prony-series are only one-term series and span low frequency ranges, with the major exceptions of ADAPT [57], ANISO KTH v1 [58], ANISO KTH v2 [59], WHIM v1 [74], ICM [8] and KTH v2 [64], which use the data of Nicolle et al. [29]. Only these models are able to capture frequencies greater than 100 Hz. This limits the scope of possible applications. For example, road traffic and low-velocity missile impacts are associated with higher frequencies, on the order of 0.1–10 kHz [20]. It is worth mentioning that the data from the YEAHM model [77,78] and Khanuja & Unni model [63] is a two-term Prony-series, coming from the fit of Rashid et al. [87]. However, the decay coefficients $\beta_1 = 38.895$ Hz and $\beta_2 = 38.911$ Hz for this series are so close that an extended frequency range was also used to match a one-term Prony-series. Ignoring the extended range of the fit from Nicolle et al. [29], the data lies in the region of $t \in [10^{-3}, 10^{0}]$. Looking at Fig. 7a, the data used by the Tse et al. and ULP v0 models [68,71] and the models of Cai et al. and SIMon v1 [61,66] are the outliers. The data is found to span many logarithmic decades, and shows greater variation in comparison to the review of Chatelin et al. [47] which found data varying within almost two decades ($g(t) \in [20, 8000]$). Furthermore, the data from FE models is substantially stiffer than that of experimental papers, including both those of the review of Chatelin et al., and from this work (see supplementary materials). In contrast, the experimental data found in this work compares well to that in the review of Chatelin et al., showing that it is indeed an issue associated with FE model data.

The outlier datasets of Fig. 7a are worth further discussion. First, the major outlier is the series of Tse et al. [68] and ULP v0 models [71] (light blue), which comes from the study of Shuck & Advani [79]. As already discussed, this data is substantially stiffer than the rest of the literature. Furthermore, there is a second outlier: the relaxation modulus data of Takhounts et al. [90] used in the Cai et al. and SIMon v1 [61,66] models (purple) is lower than that in the rest of the literature. In that experiment, the tissue was stored by freezing and experimented on between 3 and 24 h post-mortem. Other experimental sources used in FE models differ in this regard. For example, the experiment of Nicolle et al. [29] (used in ADAPT [57], KTHv2 [64], ANISO KTH v1 [58], ANISO KTH v2 [59], WHIM v1 [74] and ICM [8]) was conducted 24 h post-mortem and that of Rashid et al. [87] (used in the Khanuja-Unni [63] and YEAHM [77,78] models) was conducted within 8 h post-mortem. This may explain why the data of Cai et al. [61] and SIMon v1 [66] is less stiff than the series of Nicolle et al. [29]. The storage temperature is consistent with that of the other series of Rashid et al. [87] and Nicolle et al. [29], which range from 4 to 6 °C. This is important because storage temperature can have a very large impact on the stiffness of brain tissue, with lower storage temperatures leading to stiffer behaviour [52]. The temperature an experiment is conducted at is also important, with experiments conducted at room temperature showing a stiffer response than those measured at body temperature [56]. Thus, it is worth noting that whilst the experiments of Rashid et al. [87] and Takhounts et al. [90] were conducted at room temperature, the work of Nicolle et al. [29] was conducted at body temperature. Lastly, the specific region of the brain tested by Takhounts et al. [90] is not listed, but we note that the study of Nicolle et al. [29] was conducted on the corona radiata (white matter region) whilst that of Rashid et al. [87] was conducted on mixed white and grey matter samples. This may partly explain why the data of Takhounts et al. [90] appears to be an outlier.

The general disparity in the literature propagates through to the predictions of the storage and loss moduli where the same datasets are still outliers (Fig. 7b and c). In general, the storage modulus is observed to increase with frequency, as is the loss modulus. A characteristic n-shape is observed for the one-term Prony-series data predictions of the loss moduli, but this is simply due to the low order of the Prony-series and the use of an extended frequency range. For higher-term Prony-series such as that from Nicolle et al. [29], this behaviour is not observed.

Importantly, a further conglomeration of the data is observed upon computation of the inverse quality (Fig. 7d). This is a particularly important quantity to check as it is independent of the value of the instantaneous shear modulus M_0. The previous outlier datasets are found to lie within the rest of the data in terms of the inverse quality, which shows that the previous differences were predominantly due to their values for M_0. Oscillations in the inverse quality are also observed, which occurs due to a limited number of relaxation mechanisms in the Prony-series [122,123]. Approximately constant qualities are also anticipated due to the commonly used assumption of constant quality that is often made for determining regions of interest, as long as the dispersion is small [124].

A number of Prony-series predict extremely high wave speeds $c(\omega)$ of over 10 m/s (Fig. 7e), despite the fact that experiments have not observed speeds this high [17,125]. These predictions occur in the cases of series derived from the data of Nicolle et al. [29], and for the data of Tse et al. and ULP v0 models [68,71], both of which have large instantaneous shear moduli. As evident from Eq. (22), the wave speed scales linearly with the instantaneous shear modulus, which leads to the observed high wave speed predictions. Despite all of this variation, the derived attenuation laws in Fig. 7f are indeed generally observed to follow the expected power-law attenuation behaviour.

4.3. Attenuation power-laws in heterogeneous brain

We discuss both FE data and experimental data predictions for the regions of the heterogeneous brain collected during our literature review.

Following the same process shown for the homogeneous brain data of FE models, we computed averaged attenuation power-laws for twelve different regions in the brain, using Prony-series from FE models and from recent experimental papers. This yields averaged attenuation power-laws and frequency intervals over which the fit is valid. Both FE model data and experimental paper data were not always available for the all regions, but it was nonetheless possible to compare a number of key regions, as depicted in Fig. 8. Detailed calculations for each region are provided in the supplementary materials. Also, note that the frequency axis is not the same for the tissue types as it is dependent on the Prony-series.

Figure 8 a shows the average attenuation law in the homogeneous brain tissue in FE models and the experiments together with a “reference” power-law for homogeneous brain tissue we have used in our nonlinear (shock) shear wave modelling [17]. The “reference” was obtained using ultrasound shear wave imaging experiments performed on ex vivo porcine brain tissues [12]. The homogeneous brain tissue assumption is the most commonly used in FE modelling, meaning most data used in FE implementations comes from this region (12 unique Prony-series). For experimental data, 18 unique Prony-series were sourced for the homogeneous brain and this was not the most common tissue. As evident, the “brain-FE” law is significantly lower than the “brain” synthesised from the experimental data only. In fact, a relative error calculation between the power-law attenuation of experimental data and FE models, calculated as $\dfrac{\left(a_{\mathrm{Exp}}\omega^{b_{\mathrm{Exp}}} - a_{\mathrm{FE}}\omega^{b_{\mathrm{FE}}}\right)}{a_{\mathrm{Exp}}\omega^{b_{\mathrm{Exp}}}} \times 100$, gives a range of errors of 43–52% between 10 and 100 Hz, respectively. This suggests the need to revisit the viscoelastic modelling of brain matter in FE models to accurately capture the recent experimental data. The underestimation of attenuation in the FE implementation in contrast to experimental data is consistent in all the tissue types

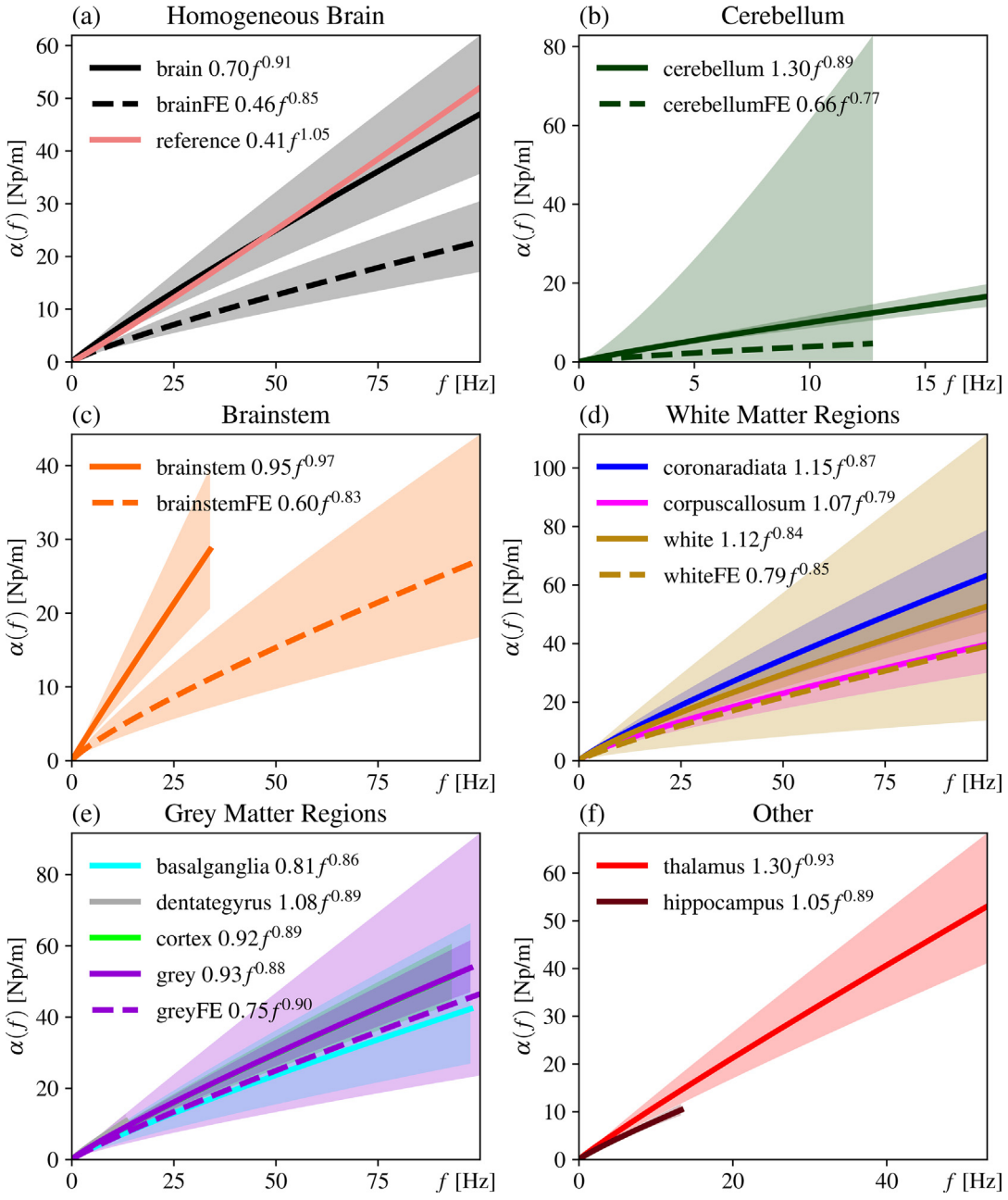

Fig. 8. Averaged attenuation power-laws at low frequencies ($<$ 100 Hz) for twelve different regions of the brain. Dashed lines refer to fits obtained from data used in FE models. Fits are only plotted over their respective valid frequency ranges. Shaded regions show one standard deviation $\pm 1\sigma$. Plotted are (a) the homogeneous brain, (b) cerebellum, (c) brainstem, (d) white matter, (e) grey matter and (f) thalamus and hippocampus regions.

and the animal types. The lower attenuation in FE models tends to predict higher stiffness in contrast to the experimental data.

Surprisingly, the experimental power-law closely aligns with the power-law attenuation we have used in our simulation studies [17]. This could possibly be due to increased emphasis on high strain rate experiments in recent publications.

Furthermore, there is also a greater degree of variation for FE model data, indicated by the larger ranges of uncertainty. The largest degree of uncertainty was found for the cerebellum region (Fig. 8b). This is not unexpected due to the lack of viscoelastic data in the FE model literature for the cerebellum region (4 unique Prony-series). For all regions except the brainstem and homogeneous brain (Fig. 8c), we observed that the fits from the experimental data lie within the error interval for the associated FE data. There are a number of possible reasons that may explain this. Firstly, as summarised in Table 2, the data used in FE models for the homogeneous brain largely comes from older viscoelastic sources, which give stiffer material properties compared to recent experimental sources. Thus, for the homogeneous brain, it is unsurprising that FE models have significantly less attenuating power-laws compared to recent experimental data. The question therefore becomes why we do not observe significant differences for other regions. The reasons for this may be that the data for FE models is newer for these regions since heterogeneity is only implemented in recent FE models. Furthermore, there is not much data for these regions, which leads to larger error intervals and thus less significant results – specifically, from FE models there are only 6 unique Prony-series for white matter, 5 for grey matter and 4 for the cerebellum. By contrast, for the homogeneous brain, there are 12 unique Prony-series.

For the white matter in particular, we point out that the power-laws in Fig. 8d for the corona radiata and corpus callosum are distinct (do not lie within the error regions of one another), but both of them lie within the error region for the white matter as used in FE models. This underlines the importance of considering heterogeneity in FE models, instead of just white matter as a whole. For comparison purposes, the corpus callosum data and corona radiata data were also pooled to create a single white matter region from experimental data, and this was found to also agree with the white matter data used in FE models. Similarly for grey matter in Fig. 8e, we found that the subregions of the basal ganglia, dentate gyrus and cortex all agreed with the grey matter data used in FE models. Moreover, the pooled data of the basal ganglia, dentate gyrus and cortex was used to generate a single grey matter region from experimental data and this was also found to agree with the data used for grey matter in FE models. For two regions, namely the thalamus and the hippocampus (Fig. 8f), no reasonable comparison was possible with other FE model data since, to the best of our knowledge, these regions have not been modelled as viscoelastic materials in the FE models considered in this work. However, it is apparent that the thalamus is found to be the most attenuating region here and thus is mechanically different from other regions. This suggests that the thalamus is an important region to include in FE models, and should not be neglected.

4.3.1. Homogenisation of attenuation in brain

We investigate if it is possible to reconstruct the homogeneous brain attenuation predictions using heterogeneous brain data. It is important to test the validity of homogeneous brain measurements, because the brain is a highly heterogeneous tissue [6,39,82,86,112–115,126]. In fact, one the key challenges identified in current FE modelling is the obtention of accurate heterogeneous data for models [4,5]. To this end, we pooled (referred as "all") the experimental data for all regions except the homogeneous brain to reconstruct the power-law for the homogeneous brain from heterogeneous brain data. This was used to quantify the the variation in the power-law resulting with the assumption of homogeneous brain and the one constructed using the heterogeneous data. The results of these processes are shown in Fig. 9.

As expected, different tissue types in brain have different power-laws and the homogeneous brain power-law (black curve) lies in between the different laws as seen in Fig. 9a. Note these laws are generated using the experimental data (has no contribution from data collected from FE models). Also interesting to note is that the power-law description for white and grey matter are almost overlapping as evident from Fig. 9a (see Table 3 for exact expressions). However, the Prony-series representation (for example: [25,127]) of these two regions are not as similar as their power-laws. The reason for this overlap could be due to our averaging procedure over different experimental procedures, tissue types, temperature, animals, etc. are used in studies on white matter versus those on grey matter. Nevertheless, such an averaging is required in order to compare and leverage different experiments and to have some starting point for modelling nonlinear shear waves in brain. On the other hand, there have been discussions around the variations in elastic and anisotropic properties of white and grey matter. Many studies report conflicting results on the anisotropy of white matter (further discussion can be found in Budday et al. [39]) and on which tissue is stiffer (discussed in Zhang et al. [128]).

Furthermore, we found that the "all" data (light blue) does not match the homogeneous brain data (solid black) as shown in Fig. 9b as well as the "reference" (light red), however, they are all still within each others' $\pm\sigma$. This difference could be due to the sampled regions for the homogeneous brain fits versus those of the rest of the experimental data. For example, the most common region found in our literature review is the cortex (43 unique Prony-series). However, since the locations for the homogeneous brain data are not explicitly given, it was not possible to determine whether the homogeneous brain data is dominated by the cortex data. However, this result nonetheless highlights a current discrepancy in the literature. It furthermore emphasises the need for considering the heterogeneity of the brain as opposed to attempting to construct a suitable averaged region, which can be highly subjective due to different averaging techniques. However, these three curves: "reference", "all", or the homogeneous "brain" fit from experimental data are not within the error region of the the attenuation power-law from FE models (dashed black). A relative error $\frac{\left(a_{\mathrm{Hom}}\omega^{b_{\mathrm{Hom}}} - a_{\mathrm{All}}\omega^{b_{\mathrm{All}}}\right)}{a_{\mathrm{Hom}}\omega^{b_{\mathrm{Hom}}}} \times 100$ of 29–39% between the homogeneous brain and the "all" region from 10 to 100 Hz also indicates a discrepancy between the heterogeneous and homogeneous treatments of brain tissue. Similarly, a relative error of 43–52% was found between the power-law attenuation of experimental data and FE models from 10 to 100 Hz, highlighting the need to revisit the viscoelastic modelling of brain matter in FE models to accurately capture recent experimental data.

4.3.2. Intra-layer variability

We discuss the variation within different tissues of the heterogeneous brain.

As can be clearly seen in Fig. 9a and Fig. 8, differing levels of intra-layer variability were also observed for different tissues. Large degrees of variation were observed for regions with little data, such as the basal ganglia (6 Prony-series) and the thalamus (11 Prony-series). This high uncertainty is simply a consequence of limited data. Of greater interest is the variation in other tissues where large numbers of data ($\geq$ 17 Prony-series) are available. For example, as depicted in Fig. 9a, larger degrees of variation are observed for the homogeneous brain ($\sigma_{\ln a} = 0.09$ and $\sigma_b = 0.03$), corpus callosum ($\sigma_{\ln a} = 0.10$ and $\sigma_b = 0.03$) and corona radiata ($\sigma_{\ln a} = 0.09$ and $\sigma_b = 0.02$), with smaller variations found for the cortex ($\sigma_{\ln a} = 0.05$ and $\sigma_b = 0.02$), grey matter ($\sigma_{\ln a} = 0.05$ and $\sigma_b = 0.01$) and white matter ($\sigma_{\ln a} = 0.07$ and $\sigma_b = 0.02$) regions. The smaller variation for the white matter region is due to the aggregation of two relatively mechanically close regions of the corona radiata and corpus callosum, as shown in Fig. 8d, leading to a lower variation in the new unified region. Similarly, low variation is also found for the grey matter for the same reason (see Fig. 8e), particularly given the low variation in the cortex region, which is the most experimentally measured tissue in our review with 43 Prony-series. However, greater degrees of variation are found for the corpus callosum and corona radiata regions. This is possibly due to variations in the experimental literature in terms of surrogate tissues used, with human, pig, cow, sheep, rat and dog surrogates used, and also due to the large degree in variation in instantaneous shear moduli, with values ranging from approximately 100 Pa to 60 kPa for both tissues. Large variation is also observed for the homogeneous brain tissue due to different testing locations, and due to the fundamentally heterogeneous nature of the brain tissue. As previously mentioned, additional variations due to different experimental protocols can also be present.

For completeness, the data for the fits for the experimental data and from FE model data are given for each region, and are shown in Tables 3 and 4, respectively. We have provided further details such as the raw data, full calculations and merged fits for each region in the supplementary materials.

Remark. Different Prony-series $g(t)$ are possible depending on the curve fitting procedure used. As a result we recommend users undertake their own curve fitting, but nonetheless we do provide our results in Tables 3, 4 and in the supplementary materials.

Table 3
Derived averaged attenuation power-laws and corresponding Prony-series from averaged experimental data. #Prony-series refers to the number of *unique* Prony-series. $M_0(\omega_0)$ is the instantaneous shear modulus obtained from a reference frequency of 75 Hz i.e. $\omega_0 = 150\pi$ Hz. The white region is formed from merging the corona radiata and corpus callosum regions, and the grey region is formed from merging the cortex, dentate gyrus and basal ganglia regions.

Region (#Prony-series)	Angular Frequency Range [Hz]		Power-law [Np/m] $\ln\alpha = \ln a + b\ln\omega$			Averaged Prony-series $\hat{g}(t) = \hat{M}_\infty + \sum_j \hat{M}_j e^{-\beta_j t}$	$\boldsymbol{M}_0(\omega_0)$ [Pa]
			Var	Val-($\mu \pm \sigma$)	95% C.I.		
Basal ganglia (6)	$\omega_{\min}$	2×10^{-5}	$\ln a$	-1.80 ± 0.21	$(-2.21, -1.40)$	$0.012 + 0.0115e^{-4.14e-05t} + 0.0174e^{-0.000381t} + 0.0303e^{-0.00331t} + 0.056e^{-0.0323t} + 0.106e^{-0.379t} + 0.216e^{-5.82t} + 0.551e^{-179t}$	4603
	$\omega_{\max}$	6.1×10^2	b	0.86 ± 0.04	(0.79,0.94)		
Brain (18)	$\omega_{\min}$	0.01	$\ln a$	-2.03 ± 0.09	$(-2.21, -1.85)$	$0.0902 + 0.0608e^{-0.0223t} + 0.0952e^{-0.291t} + 0.193e^{-4.88t} + 0.561e^{-180t}$	4607
	$\omega_{\max}$	7.3×10^2	b	0.91 ± 0.03	(0.86,0.97)		
Brainstem (23)	$\omega_{\min}$	0.0048	$\ln a$	-1.83 ± 0.11	$(-2.04, -1.62)$	$0.0988 + 0.05e^{-0.0104t} + 0.0774e^{-0.131t} + 0.163e^{-1.97t} + 0.611e^{-55.8t}$	4430
	$\omega_{\max}$	2.1×10^2	b	0.97 ± 0.04	(0.89,1.05)		
Cerebellum (18)	$\omega_{\min}$	0.0061	$\ln a$	-1.36 ± 0.06	$(-1.48, -1.24)$	$0.0502 + 0.0455e^{-0.0122t} + 0.0782e^{-0.124t} + 0.177e^{-1.5t} + 0.649e^{-32.6t}$	4417
	$\omega_{\max}$	1.1×10^2	b	0.89 ± 0.02	(0.84,0.93)		
Corona radiata (19)	$\omega_{\min}$	0.0016	$\ln a$	-1.46 ± 0.09	$(-1.62, -1.29)$	$0.00544 + 0.00509e^{-0.00298t} + 0.00829e^{-0.0271t} + 0.0168e^{-0.272t} + 0.0361e^{-3.49t} + 0.0977e^{-57.5t} + 0.213e^{-3.2e+03t} + 0.618e^{-8.98e+04t}$	24277
	$\omega_{\max}$	10^5	b	0.87 ± 0.02	(0.83,0.91)		
Corpus callosum (17)	$\omega_{\min}$	0.00099	$\ln a$	-1.38 ± 0.10	$(-1.57, -1.19)$	$0.00934 + 0.016e^{-0.00227t} + 0.0359e^{-0.0215t} + 0.0933e^{-0.246t} + 0.249e^{-4.23t} + 0.597e^{-173t}$	4596
	$\omega_{\max}$	6.6×10^2	b	0.79 ± 0.03	(0.73,0.84)		
Cortex (43)	$\omega_{\min}$	2×10^{-5}	$\ln a$	-1.71 ± 0.05	$(-1.82, -1.60)$	$0.013 + 0.0101e^{-3.59e-05t} + 0.0147e^{-0.000319t} + 0.0261e^{-0.00296t} + 0.0472e^{-0.0317t} + 0.0874e^{-0.369t} + 0.19e^{-5.45t} + 0.612e^{-171t}$	4593
	$\omega_{\max}$	5.8×10^2	b	0.89 ± 0.02	(0.85,0.92)		
Dentate gyrus (7)	$\omega_{\min}$	0.079	$\ln a$	-1.55 ± 0.06	$(-1.68, -1.43)$	$0.116 + 0.104e^{-0.17t} + 0.189e^{-1.96t} + 0.592e^{-35.3t}$	4418
	$\omega_{\max}$	83	b	0.89 ± 0.03	(0.84,0.94)		
Grey (56)	$\omega_{\min}$	2×10^{-5}	$\ln a$	-1.69 ± 0.05	$(-179, -1.61)$	$0.0122 + 0.00968e^{-3.61e-05t} + 0.0142e^{-0.000321t} + 0.0255e^{-0.00299t} + 0.0466e^{-0.0323t} + 0.0867e^{-0.379t} + 0.189e^{-5.62t} + 0.616e^{-179t}$	4609
	$\omega_{\max}$	6.1×10^2	b	0.88 ± 0.01	(0.86,0.91)		
Hippocampus (18)	$\omega_{\min}$	0.01	$\ln a$	-1.58 ± 0.04	$(-1.67, -1.50)$	$0.0874 + 0.0892e^{-0.0291t} + 0.192e^{-0.534t} + 0.631e^{-18.5t}$	4412
	$\omega_{\max}$	83	b	0.89 ± 0.02	(0.86,0.92)		
Thalamus (11)	$\omega_{\min}$	0.0047	$\ln a$	-1.46 ± 0.08	$(-1.62, -1.29)$	$0.0493 + 0.0344e^{-0.0105t} + 0.0594e^{-0.134t} + 0.144e^{-2.16t} + 0.713e^{-82.4t}$	4454
	$\omega_{\max}$	3.3×10^2	b	0.93 ± 0.03	(0.88,0.99)		
White (36)	$\omega_{\min}$	0.0099	$\ln a$	-1.43 ± 0.07	$(-1.56, -1.30)$	$0.0043 + 0.00473e^{-0.0017t} + 0.00772e^{-0.013t} + 0.0154e^{-0.105t} + 0.0307e^{-0.992t} + 0.0559e^{-9.94t} + 0.101e^{-99.5t} + 0.227e^{-1.58e+03t} + 0.554e^{-3.77e+04t}$	4609
	$\omega_{\max}$	10^5	b	0.84 ± 0.02	(0.80,0.87)		

Table 4
Derived averaged attenuation power-laws and corresponding Prony-series from averaged FE model data. #Prony-series refers to the number of *unique* Prony-series. $M_0(\omega_0)$ is the instantaneous shear modulus obtained from a reference frequency of 75 Hz i.e. $\omega_0 = 150\pi$ Hz.

Region (#Prony-series)	Angular Frequency Range [Hz]		Power-law [Np/m] $\ln\alpha = \ln a + b\ln\omega$			Averaged Prony-series $\hat{g}(t) = \hat{M}_\infty + \sum_j \hat{M}_j e^{-\beta_j t}$	$\boldsymbol{M}_0(\omega_0)$ [Pa]
			Var	Val-($\mu \pm \sigma$)	95% C.I.		
Brain (12)	$\omega_{\min}$	6.7	$\ln a$	-2.32 ± 0.13	$(-2.58, -2.07)$	$0.312 + 0.148e^{-9.73t} + 0.141e^{-84.3t} + 0.178e^{-871t} + 0.22e^{-3.01e+04t}$	6780
	$\omega_{\max}$	10^5	b	0.85 ± 0.02	(0.80,0.89)		
Brainstem (4)	$\omega_{\min}$	3.4	$\ln a$	-2.03 ± 0.20	$(-2.42, -1.63)$	$0.222 + 0.145e^{-5.48t} + 0.157e^{-48.7t} + 0.228e^{-587t} + 0.248e^{-2.77e+04t}$	6967
	$\omega_{\max}$	10^5	b	0.83 ± 0.04	(0.74,0.91)		
Cerebellum (4)	$\omega_{\min}$	3.3	$\ln a$	-1.82 ± 0.82	$(-3.42, -0.22)$	$0.525 + 0.475e^{-18.3t}$	4412
	$\omega_{\max}$	80	b	0.77 ± 0.47	$(-0.15, 1.69)$		
Grey (5)	$\omega_{\min}$	3.3	$\ln a$	-1.94 ± 0.21	$(-2.36, -1.52)$	$0.264 + 0.219e^{-8.65t} + 0.517e^{-183t}$	4606
	$\omega_{\max}$	700	b	0.90 ± 0.07	(0.76,1.04)		
White (6)	$\omega_{\min}$	13	$\ln a$	-1.80 ± 0.33	$(-2.45, -1.14)$	$0.484 + 0.516e^{-45.5t}$	4423
	$\omega_{\max}$	700	b	0.85 ± 0.11	(0.63,1.06)		

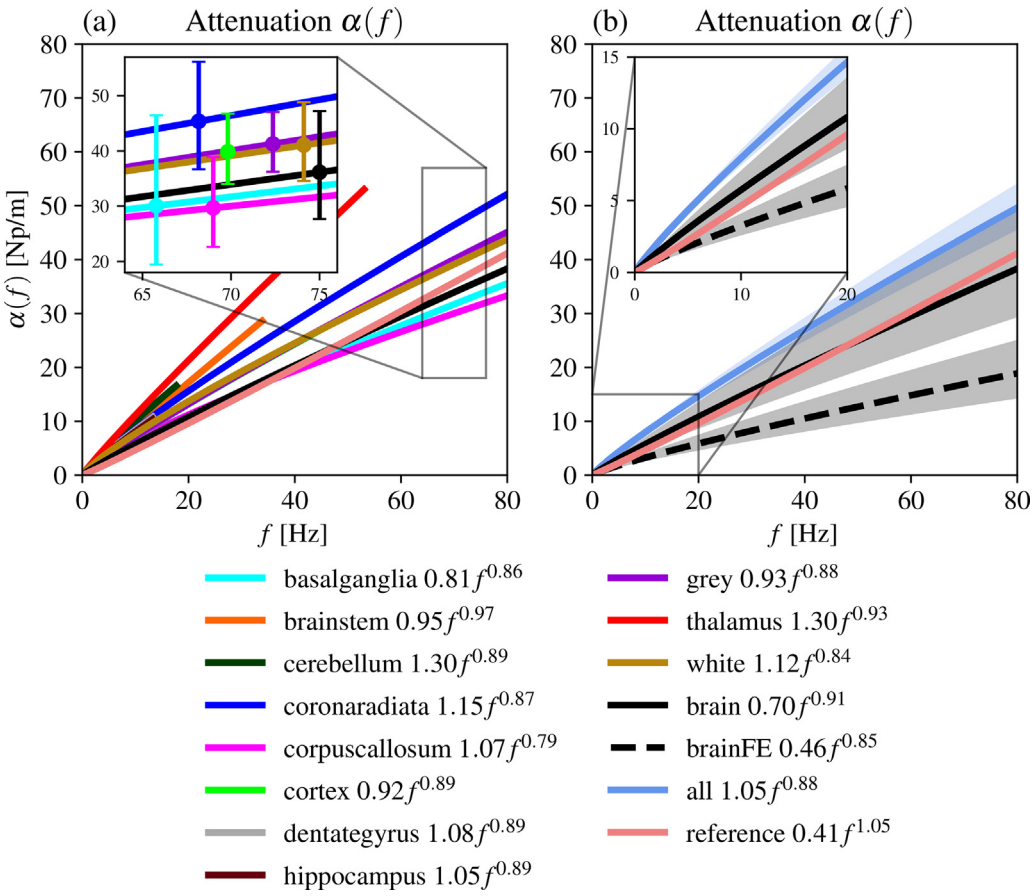

Fig. 9. Attenuation power-laws at low frequencies (< 80 Hz) for experimental data. The "all" fit is generated from merging the data for all regions bar the homogeneous brain (i.e. hippocampus, thalamus, brainstem, cerebellum, grey matter and white matter). Shaded regions show one standard deviation $\pm 1\sigma$, as do error bars. Depicted are: (a) the power-law attenuation fits from experimental data for all of the gathered regions and (b) the power-law attenuation fits for the homogeneous brain (both FE and experimental), and the "all" region (solely experimental). The reference law of Tripathi et al. [17] is also shown for comparison in (b), alongside the average homogeneous brain attenuation from FE models (shown as a dashed black line).

4.4. Variation in attenuation due to animal selection

We investigate differences between surrogate tissues in the experimental literature. There are multiple factors that can cause differences in experimental results, but one that is of key importance is that of the suitability of surrogate animals. The influence of this factor is vital to check because fresh human brain tissue is far more difficult to source than tissue from other animals such as pigs or cows. Thus, it is necessary to ascertain if surrogate tissues can be used since this will have major ramifications on the ease of obtention of suitable experimental data.

Experiments have already investigated this question, but only on a per-experiment basis. For example, MacManus et al. directly compared fits for human, pig, rat and mouse brains using indentation techniques [129]. Nicolle et al. similarly compared porcine tissue to human tissue using oscillatory experiments [20]. Here we review across multiple experiments, specifically, we investigate the averaged properties from a large experimental literature segregated by animal type and region as shown in Fig. 10.

To achieve this, we employ the same methodology as was done for the homogeneous brain characterisation used in FE models. For these comparisons, the following regions were considered: homogeneous brain, cerebellum, brainstem, white matter (i.e. corpus callosum and corona radiata data merged), grey matter (i.e. dentate gyrus, cortex and basal ganglia data merged) and "all" region created by merging data from all regions i.e. hippocampus, thalamus, brainstem, cerebellum, grey matter and white matter except the homogeneous brain. A total of eight different animals were found in our literature review - namely, pig, rat, human, mouse, cow, sheep, monkey and dog. However, due to scarcity of data from monkeys, sheep and dog, are not shown in Fig. 10.

Our results found that the average power-laws for each surrogate tissue do not always agree. That is, the variation in results with respect to the use of different surrogate tissues is in fact significant. This finding is not unexpected. For example, differences between human tissue and rodent brain tissue are anticipated since the rodent brain is quite anatomically different from the human brain [114]. Even for more anatomically similar tissues such as porcine and bovine tissue, differences are still observed in this work. We do however still note that there are other sources of variation due to different experimental techniques, post-mortem time, temperature, etc. that are also present in our dataset. For example, the data on human tissue comes primarily from indentation experiments [23,129–131] whilst for bovine tissue it primarily comes from dynamic mechanical analysis [108]. Thus, we can anticipate that differences between the bovine dataset and human dataset will also occur due to differences in testing methods.

We also point out some general trends observed here. We can see that the experimental data from human tissue is in fact generally less attenuating than porcine tissue, but more attenuating than bovine tissue, as can be observed for the homogeneous brain region (Fig. 10a), white matter (Fig. 10d), grey matter (Fig. 10e), and the "all" region (Fig. 10f). Rat and mouse tissues were found to be close. Like in the previous section, here also we calculate the

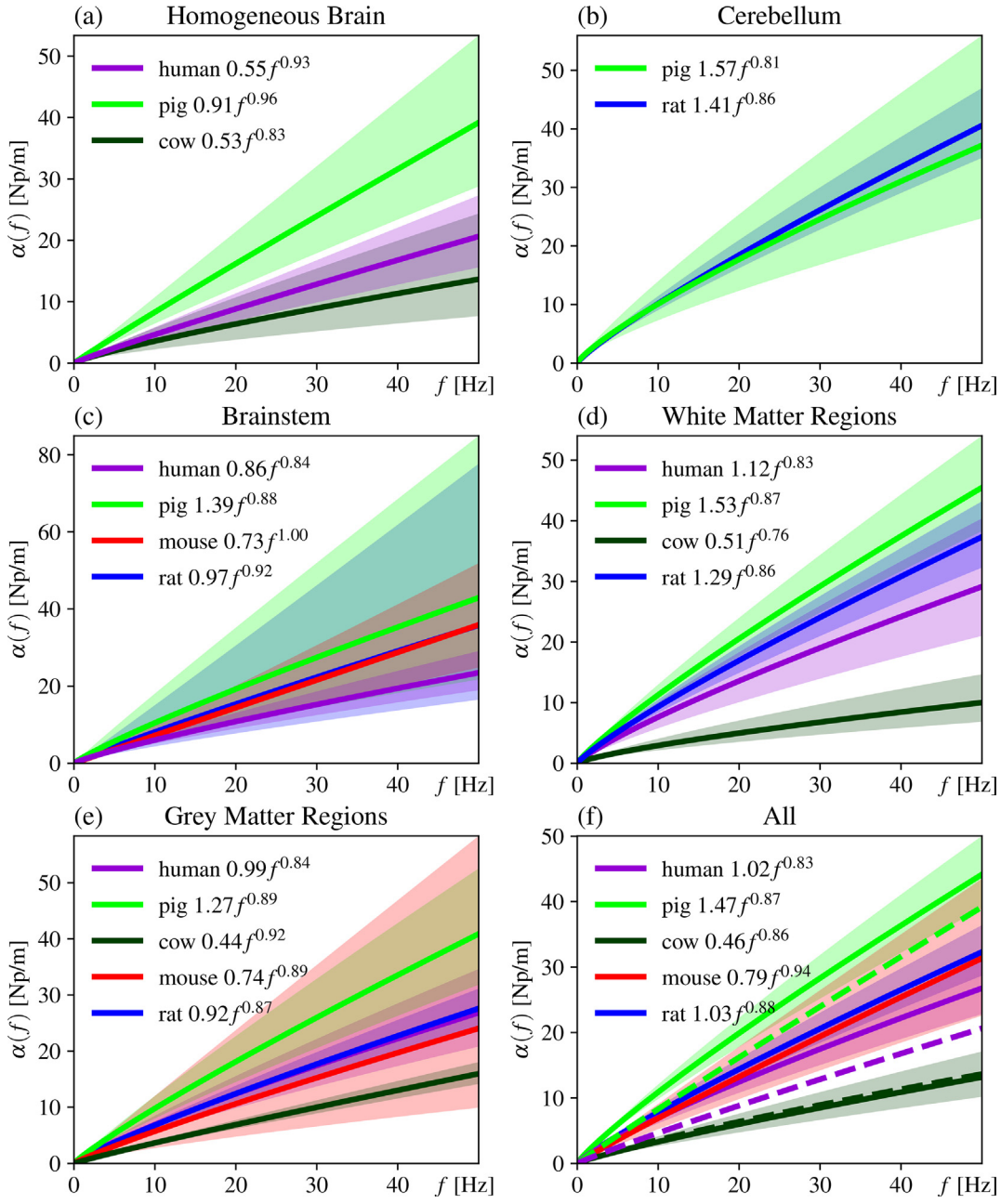

Fig. 10. Averaged attenuation power-laws in a low frequency regime (0–50 Hz) for a number of key regions, separated by animal type. The "all" fit is generated from merging the data for all regions bar the homogeneous brain (i.e. hippocampus, thalamus, brainstem, cerebellum, grey matter and white matter). Shown are the attenuation power-law fits from experimental data for the different animal types for (a) the homogeneous brain, (b) cerebellum, (c) brainstem, (d) white matter, (e) grey matter and (f) "all" regions. Shown with a dashed line in subplot (f) are the fits from the homogeneous brain data as shown in subplot (a).

power-laws for the "all" region and the homogeneous brain, which are similar for the various animal types (Fig. 10f). This is a promising finding since exact agreement is not expected - the data for the "all" region may be skewed towards various subregions depending on the data we have sourced. For example, 27% of the data for rat comes from the cortex region.

It is particularly interesting to note that in this study the fits for larger animals such as porcine and bovine tissue were also found in general to be further from the fits for human tissue as compared to the fits for smaller animals such as rats and mice. This finding seems in direct conflict with the work of Dai et al. [46], who recommend the use of larger animals such as cows and pigs as surrogates over small animals such as rodents. However, there exists other work such as that of MacManus et al. [129] which suggest that mouse tissue is in fact a suitable surrogate.

Furthermore, there are a number of reasons why we may observe this in this work. For one, it is important to keep in mind that there is relatively little data for rat and mouse brains, and the data that is presented lies in the low frequency regime (<10 Hz). As a result, the extrapolation to 50 Hz is exactly that: only an extrapolation. Thus, any comparisons at higher frequencies should be done carefully. Furthermore, we also point out that the cortex region is also the most commonly experimented upon tissue for the rat, mouse and human data, whilst this is not the case for the porcine and bovine tissues. These differences in sampled subregions of the brain may also partly explain the trends observed in this work. However, this still does not fully explain why the porcine tissue seems to be substantially more attenuating than other tissue types. This phenomenon instead appears to come due to different experimental techniques. In the collected literature,

the dominant experimental technique for porcine tissue is indentation tests [86,111,126,132–134]. This is also a common experimental technique for other surrogates such as rat also, but the experimental results for porcine tissues are substantially different. Specifically, there is a disproportionate amount of experiments on porcine tissue in the literature that find low instantaneous shear moduli, which leads to high predictions for the attenuation. For example, of all the Prony-series data collected for porcine tissue, 55% of the pig data has an instantaneous shear modulus less than 1500 Pa. By contrast, for rat tissue it is merely 23% and for human it is 33%. This difference does not appear amongst experiments which have conducted experiments on both porcine and other surrogates using the same experimental procedure [20,129]. Instead, this arises from the fact that there are experiments conducted *solely* on porcine tissue which report low values for the instantaneous shear modulus [48,96,111,135–138]. In particular, this finding emphasises that the use substitute data from surrogate tissues must be done with much caution.

4.5. Limitations and shortcomings

This study does have some limitations. First, the reference values were not varied per region in this work and we took $\rho = 1000$ kg/m^3 and $c = 2.1$ m/s at 75 Hz for all regions and has been fixed for M_0 calculations. The use of a constant density is in line with the approach of FE models but is nonetheless limiting. The reference dispersion value is obtained with the assumption of homogeneous brain tissue. Thus, it may not be suitable for tissues that are very different from the homogeneous brain like meninges and spine. We were unable to include these tissues as a result, although there does exist experimental Prony-series data for them (see [103–105,139–142]).

Another key issue is the variations of the experimental datasets in the literature. Since there are many possible sources of variation, it is not feasible to account for all of them at the present time, particularly given that the literature does not agree on how to quantify their effects. For example, there is even some dispute about the existence of certain effects such as the sex-dependence of brain tissue properties [39]. Other studies investigating various experimental conditions are also with limitations. For example, one of the few studies into the temperature dependence was conducted by Hrapko et al. [56], but considered just 5 different temperatures between 7 °C and 37 °C and only considered homogeneous porcine brain tissue. As a result, it is not feasible to accurately account for all the effects of various experimental conditions here. It is hoped that by averaging across many series in this work, the variations will even out to some degree. Nevertheless, FE models use data from a wide range of experimental sources, often with large differences in experimental conditions and parameters. In order to compare and review such FE data, it is therefore a necessary limitation to also compare and aggregate experimental data from such varying sources.

Thirdly, the reliance on Prony-series data is also limiting, particularly when considering frequency-domain quantities. As mentioned previously, the use of a limited number of mechanisms in a Prony-series causes oscillatory artefacts to appear in the predicted inverse quality [122,123]. Thus, it would be better to directly use data from the frequency domain for such quantities, but this is not what current FE models are predominantly doing. Furthermore, during the literature it was found that more experimental papers yielding Prony-series data were available as compared to frequency-domain data. As a result, this was a necessary limitation to introduce to this work. Similarly, the curve fitting of a Prony-series is also limiting but necessary in order to give results that can be used by FE models. Nonetheless, we also provide the direct power-law fit so frequency-domain data is also available in this work.

It is vital to stress that curve fitting for Q^{-1} is a difficult exercise and greatly differing fits can be obtained for the same data depending on the chosen algorithm and initial conditions [27]. As a result, we recommend that users conduct their own curve fitting exercises which they can tailor specifically to their application. To facilitate this, we provide the averaged power-laws used to derive our Prony-series. We emphasise that these power-laws should be treated as the ground truth as opposed to the averaged Prony-series.

It is also important to note, in the backward calculation, due to fixed reference dispersion value in the Kramers-Kronig relation it is not always able to produce a reconstructed dispersion curve consistent with the Prony-series predictions. This is also due to the limiting nature of the Kramers-Kronig relation and also due to factors like heterogeneity, experimental technique, physical parameters like temperature, etc. (see appendix for further discussion).

Lastly, the initial Prony-series are not exact measurements, and should have errors associated with them. Unfortunately, errors were not available for all Prony-series, so it was not feasible to utilise such information in this work.

4.6. Recommendations for future work

The dominant method of modelling viscoelasticity for current state-of-the-art FE models is by means of a Prony-series, though some models, such as the LiUHead model [143], have opted for other approaches. This state of affair is unlikely to change in the immediate future, but there are a number of improvements we can suggest to current techniques.

First, many FE models are incorporating viscoelasticity by means of a one-term Prony-series [144], which greatly limits the frequency range that can be modelled, especially if one is interested in modelling the transient viscoelastic behaviour. There also exists a large range of higher order viscoelastic models in the literature which are included in this work and these laws could be leveraged instead.

Furthermore, this work and many others [6,25,39] have established that the brain is heterogeneous, whilst it is often times treated as a homogeneous tissue. In some cases, properties for certain tissues as used in FE models have also been derived from experiments on different tissues - for example, the homogeneous brain properties of the ADAPT [57], ANISO KTH v1 [58], ANISO KTH v2 [59], WHIM v1 [74], ICM [8] and KTH v2 [64] models are taken from experiments by Nicolle et al. [29] on corona radiata tissue. Similarly, the homogeneous brain properties derived from the experiments of Shuck & Advani [79] are also derived from corona radiata tissue. This is could lead to erroneous results and should be used with caution.

There are also differences between the tissues chosen for inclusion in FE models versus the tissues that are experimented on. Experiments can provide different measurements for specific regions compared to the larger regions taken by FE models. For example, the cortex region which is sometimes included in FE models is measured in a total of six subregions by Menichetti et al. [130] - namely the prefrontal cortex, posterior-occipital cortex, superior mid-frontal cortex, postero-lateral frontal cortex, inferior temporal cortex and the postero-superior frontal cortex. A clear difference is also that FE models are currently often modelling the two regions of white and grey matter whilst typically experimental papers are not. Instead, a significant amount of experimental work measures subregions of these - white matter is commonly measured as either the corona radiata or the corpus callosum, and grey matter as the basal ganglia, cortex or the dentate gyrus. Furthermore, our work has found that these subregions are mechanically different

(see Fig. 8). Thus, these subregions should be considered separately in future work.

We also point out that taking viscoelastic and hyperelastic data from different experiments can be problematic as viscoelastic fits can change depending on the hyperelastic model used, and also vary in general between experiments. Our work also shows that experimental data and data used in FE models do not agree with each other. Thus, we recommend using directly experimental measurements in future work as opposed to modifying or scaling experimental data. In this work we provide both averaged laws for twelve regions and eight different animals and also a total of 181 different Prony-series in order to facilitate this. Furthermore, as was mentioned in the limitations section, the use of Prony-series is not ideal. Future work could directly obtain averaged laws from frequency-domain data i.e. values of M' and M''.

Another important area of future investigation is the incorporation of probabilistic modelling. Currently, our approach characterises the error in our fitted parameters simply by a single standard deviation or confidence interval. This is currently still the commonly implemented approach in giving errors for fitting Prony-series [82,107,114,145]. However, a probabilistic formulation may deliver other estimates which could be more suitable. Furthermore, a number of works now exist investigating stochastic modelling of hyperelastic models such as the Neo-Hookean model [146], Mooney-Rivlin model [146] and the Ogden model [147]. Extensions to anisotropic models have also recently been explored, for example by Chen and Guilleminot [148]. These works provide a useful new direction to explore, allowing for probabilistic representations in hyperelasticity. We believe future work could look at a probabilistic formulation for our method, providing a richer characterisation of our dataset and allowing us to determine the *distribution* of our fitted parameters. Machine learning methods such as the work of Nolan et al. [149] are of interest here, possibly allowing one to better leverage collected information such as surrogate animal and tissue type to make predictions.

Machine learning methods are also of great interest for FE modelling in general. In particular, this review has highlighted a number of issues with existing FE models, and an enormous amount of variation within the experimental literature. As a result, the best choice of material parameters is not always clear for both experimentalists and the FE modelling community. Machine learning has the possibility to revolutionise both domains. For instance, Kutz and collaborators have done significant work [150–153] in development of sparse-regression based techniques for discovery of model parameters using experimental data. Furthermore, physics-informed neural networks, which allow for the efficient evaluation of both forward and inverse problems [154–156] whilst directly embedding physics knowledge in the neural network model itself, can be a viable option. Similarly, reduced order modelling [157,158] also provides a means of efficient evaluation of parametrised partial differential equations, particularly important for real-time many-query contexts. In particular, machine-learning based reduced order modelling approaches [159–164] offer real potential to decrease the computational overhead for traumatic brain injury modelling. In addition, neural operators such as DeepONets [165–167] and Fourier neural operators [168,169] have recently arisen as a promising new means of reduced order modelling, directly learning a map between function spaces and typically benefitting from the advantageous property of discretisation-invariance [169,170]. The use of such methods is an extremely important future direction since more efficient simulations would open new avenues for the determination of appropriate material parameters by experimentalists, in addition to allowing for a better understanding of the effect of varying material parameters in FE models.

5. Conclusion

To the best of our knowledge, this work presents 1) the first multi-frequency viscoelastic atlas of the heterogeneous brain, 2) the first review focusing on *viscoelastic* modelling in *both* FE models and in experimental works, 3) the first attempt to conglomerate the disparate existing literature on the viscoelastic modelling of the brain. Thus, our review differs from existing work in a number of key ways.

Our review enables a direct comparison between the experimental literature and the data used in FE models. Existing reviews focus typically on either reviewing FE models, or reviewing experimental techniques, but not both together. This review aims to help bridge the gap between these two domains. To this end, we have gathered a total of 181 differing Prony-series from 48 different experimental papers, and 31 unique Prony-series used in FE models. We have made all of these 212 Prony-series publicly available in the supplementary materials, including information regarding the anatomical region of the brain and also the surrogate used. As such, this review gives the largest collection of viscoelastic parameters for human brain tissue. This wealth of data allows us to investigate differences due to animal tissue choices in the heterogeneous brain with greater granularity, for instance, we can now compare corona radiata of a pig brain with that of the cortex of the human brain unlike previous studies. Our work also provides a means of comparing Prony-series viscoelasticity to storage and loss moduli data (e.g. from MRE measurements), and to attenuation laws. Previous works have not thoroughly investigated the link between relaxation functions and storage and loss moduli. For example, the review of Chatelin et al. [47] provides many different experimental results for relaxation functions, and also many different distinct experimental results for storage and loss moduli. However, their review does not investigate how the predictions of the storage and loss moduli from the relaxation function compare with the other experimental data for the storage and loss moduli.

Comparison of FE model data with the recent experimental data yields that FE models are generally underestimating the attenuation than the recent experimental data. Our review uncovers that there may be issues with existing commonly used Prony-series data. For example, the most used dataset in FE models is the one presented by Shuck and Advani [79]. However, their data is much stiffer than the average calculated using our approach. They have found that for a frequency range between 3 and 300 Hz, the storage modulus lies between 7 and 30 kPa, and loss modulus lies between 1 and 90 kPa, whilst in this work our average Prony-series predicts lower values for both the storage modulus (between 1 and 6 kPa) and loss modulus (between 0.3 and 1 kPa). It is thus clear from both this work and other previous reviews such as Chatelin et al. [47] and Hrapko et al. [56] that the data of Shuck and Advani is an outlier with respect to the rest of the experimental literature. In addition, another commonly used dataset, namely that of Nicolle et al. [20] was found to predict an inverse quality greater than 1. Therefore there is a need to recalibrate and reassess the material properties used in the computational models describing the brain trauma.

We calculate the average attenuation power-law for the homogeneous brain tissue from recent experimental data (obtained from 18 unique Prony-series) as $\alpha(f) = 0.70 f^{0.91}$ Np/m. The corresponding average dimensionless Prony-series is $\hat{g}(t) = 0.0902 + 0.0608e^{-0.0223t} + 0.0952e^{-0.291t} + 0.193e^{-4.88t} + 0.561e^{-180t}$, with an instantaneous shear modulus of 4607 Pa at 75 Hz. The mean and median instantaneous shear modulus in the experimental literature are 6230 Pa and 3750 Pa, respectively.

Significant differences are also observed between the animal types, with relative errors of 23–38% between human and bovine tissue and 78–95% between human and porcine tissue for the at-

tenuation power-law fits between 10 and 100 Hz for the homogeneous brain region. This emphasises the need to take caution when using surrogate tissues, since substantial differences can exist.

In addition, this work provides a methodology for computing the predictions of a given Prony-series on the storage and loss moduli, quality factor, dispersion relation and attenuation. Since we have been able to calculate averaged Prony-series and power-laws, it also provides a useful methodology for investigating and comparing an experimentally obtained Prony-series to the rest of the experimental literature. Importantly, it is also possible to verify whether or not a Prony-series predicts an inverse quality less than 1 for it to be physically viable. Thus Prony-series which do not satisfy this may need to be recalibrated. From a numerical stand point, the methods using one- or two- term Prony-series can limit the attenuation and dispersion modelling especially in the nonlinear regime which results in the generation of higher harmonics such as shear shock formation in brain [17].

Declaration of Competing Interest

The authors declare that they have no known competing financial interests or personal relationships that could have appeared to influence the work reported in this paper.

Appendix A. Validation of averaged viscoelastic properties

Our procedure for determining averaged Prony-series data involves a number of nontrivial steps and thus it is important to verify that our method proceeds as expected. Specifically, a number of sensible checks can be conducted:

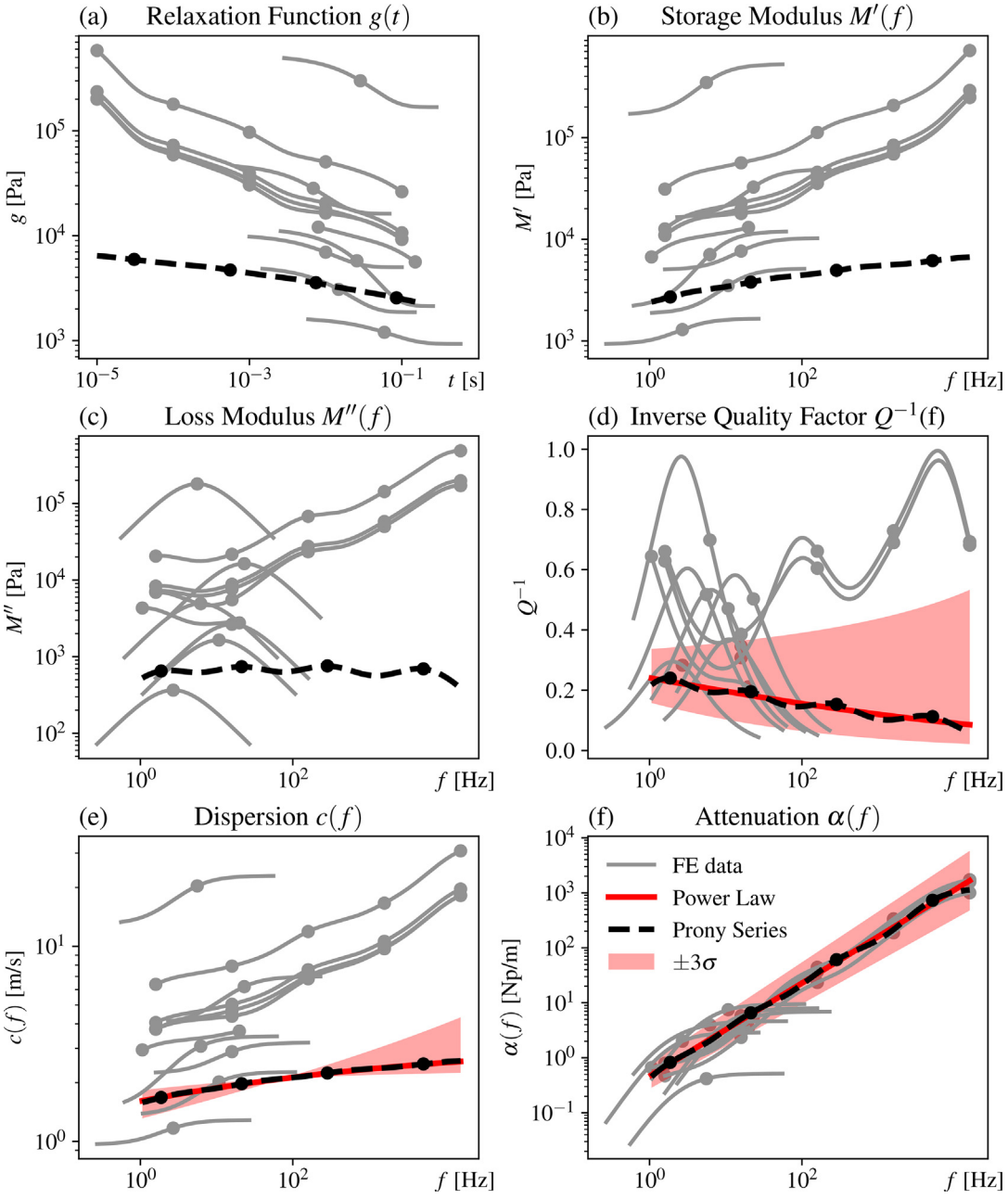

Fig. A1. Derivation of averaged attenuation power-laws, and corresponding dispersion and quality (shown in red). An averaged Prony-series and its predictions are also shown in black. Shown are the predictions for (a) the relaxation function, (b) storage modulus, (c) loss modulus, (d) inverse quality factor, (e) dispersion and finally (f) attenuation. (For interpretation of the references to colour in this figure legend, the reader is referred to the web version of this article.)

- Can our averaged Prony-series reconstruct the averaged power-law from which it was derived?
- Does our averaged Prony-series lie amongst the experimental data from which it was derived?
- Does our averaged Prony-series or attenuation power-law predict $Q^{-1} < 1$ as expected?
- Does our determined value of M_0 from our Prony-series match that of the experimental data?

We illustrate this procedure for the experimental data on the homogeneous brain tissue. Details for other tissue types can be found in the supplementary materials.

Following the obtention of an averaged Prony-series as shown in Fig. 5d, the forward calculation step can be conducted on this new Prony-series as outlined in Fig. 5e. The results of this process are shown in Fig. A.1.

As evident from Fig. A.1a, the averaged Prony-series (dashed black) calculated using $c(\omega)$ given the Kramers-Kronig relations underestimates the storage/loss modulus and the inverse quality (Fig. A.1b–e, respectively). However, it is able to reconstruct the attenuation power-law (red) shown in Fig. A.1f. The underestimation of the storage/loss modulus and the inverse quality is due to the use of Kramers-Kronig relations [31] which may not be ideal for the point estimates provided for Prony-series, moreover the use of the reference value of $c = 2.1$ m/s at 75 Hz further restricts the approximation. It can be seen in Fig. A.1e that the averaged dispersion is unable to match the predictions of the individual Prony-series. This is because the Prony-series predict extremely high dispersion values of up to 10 m/s at the reference frequency of 75 Hz. Experiments have not observed dispersion values this high, and the experimentally determined reference dispersion is only 2.1 m/s. Combined with the form enforced by the Kramers-Kronig relation, an underestimation in the dispersion compared to the individual Prony series predictions leads to an underprediction in the averaged Prony-series also. However, these predictions can vary depending on the reference parameters taken which depend on the experimental conditions like temperature, tissue type, etc. Nevertheless, this approach does provide a benchmark to unify the different observations obtained using different experimental techniques.

Lastly, we can also examine the prediction for M_0 from our averaged Prony-series, since this an important experimental quantity in the literature. It is important to determine whether or not the prediction from Eq. (31) is in line with the distribution of values of M_0 from the literature. In general, quite a lot of variation exists in the predictions for the instantaneous shear modulus since this can depend upon experimental techniques and procedures. It is not possible to experimentally measure a value for the relaxation function at $t = 0$, so differing values of M_0 can occur depending on what time interval (or frequency range) one investigates. In our work, we find our averaged Prony-series for the experimental homogeneous brain tissue has a value $M_0 = 4607$ Pa at 75 Hz. This broadly agrees with the experimental literature, which has a mean value of 6230 Pa and a median value of 3750 Pa.

Appendix B. Convergence of proposed methodology

Another important consideration is to investigate the convergence of our proposed methodology. In this section, we provide some empirical convergence results of our method as a function of the number of samples. We consider a situation in which our data may be noisy, and show that our results for the attenuation do converge. As discussed in Appendix A, results for our averaged Prony-series may not converge to the Prony-series from which they were derived due to the reference dispersion value and the form of the Kramers-Kronig relation.

To demonstrate convergence in the averaged attenuation power-law, we consider an arbitrary ground truth Prony-series data $\hat{g}(t) = \frac{1}{3}\left(e^{-1000t} + e^{-10000t} + e^{-100000t}\right)$ with $M_0 = 20000$. We then allow noise to enter the measured Prony-series. Specifically, for the parameters $\hat{M}_i$ and M_0, we draw noise from a Gaussian distribution with mean zero and a standard deviation equal to 10% of the ground truth value. Convergence in the predictions for the attenuation power-law $\alpha(\omega) = a\omega^b$ is then empirically found with increasing numbers of samples, as shown in Fig. B1.

Supplementary material

Supplementary material associated with this article can be found, in the online version, at 10.1016/j.actbio.2023.07.040.

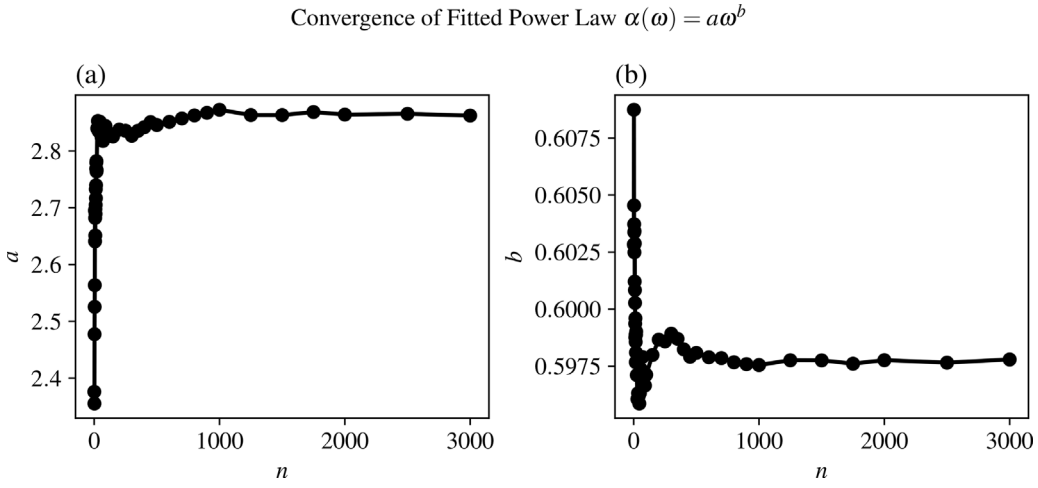

Fig. B1. Convergence in the fitted attenuation power-law parameters (a) a and (b) b.

References

[1] A. Basso, I. Previgliano, F. Servadei, Neurological disorders: a public health approach (Traumatic brain injuries), in: Neurological Disorders: Public Health Challenges, World Health Organisation, 2006, pp. 164–175.
[2] A. Gustavsson, M. Svensson, F. Jacobi, C. Allgulander, J. Alonso, E. Beghi, R. Dodel, M. Ekman, C. Faravelli, L. Fratiglioni, B. Gannon, D.H. Jones, P. Jennum, A. Jordanova, L. Jönsson, K. Karampampa, M. Knapp, G. Kobelt, T. Kurth, R. Lieb, M. Linde, C. Ljungcrantz, A. Maercker, B. Melin, M. Moscarelli, A. Musayev, F. Norwood, M. Preisig, M. Pugliatti, J. Rehm, L. Salvador-Carulla, B. Schlehofer, R. Simon, H.C. Steinhausen, L.J. Stovner, J.M. Vallat, P.V.d. Bergh, J. van Os, P. Vos, W. Xu, H.U. Wittchen, B. Jönsson, J. Olesen, Cost of disorders of the brain in Europe 2010, Eur. Neuropsychopharmacol. 21 (2011) 718–779.
[3] J.P. Mihalik, R.C. Lynall, E.B. Wasserman, K.M. Guskiewicz, S.W. Marshall, Evaluating the “threshold theory”: can head impact indicators help? Med. Sci. Sports Exerc. 49 (2017) 247–253.
[4] E. Griffths, S. Budday, Finite element modeling of traumatic brain injury: areas of future interest, Curr. Opin. Biomed. Eng. (2022) 100421.
[5] D.B. MacManus, M. Ghajari, Material properties of human brain tissue suitable for modelling traumatic brain injury, Brain Multiphys. 3 (2022) 100059.
[6] N. Antonovaite, L.A. Hulshof, E.M. Hol, W.J. Wadman, D. Iannuzzi, Viscoelastic mapping of mouse brain tissue: relation to structure and age, J. Mech. Behav. Biomed. Mater. 113 (2021) 104159.
[7] W. Zhao, B. Choate, S. Ji, Material properties of the brain in injury-relevant conditions–experiments and computational modeling, J. Mech. Behav. Biomed. Mater. 80 (2018) 222–234.
[8] M. Ghajari, P.J. Hellyer, D.J. Sharp, Computational modelling of traumatic brain injury predicts the location of chronic traumatic encephalopathy pathology, Brain 140 (2017) 333–343.
[9] T.J. Horgan, M.D. Gilchrist, The creation of three-dimensional finite element models for simulating head impact biomechanics, Int. J. Crashworthiness 8 (2003) 353–366.
[10] I. Cinelli, M. Destrade, P. McHugh, A. Trotta, M. Gilchrist, M. Duffy, Head–to-nerve analysis of electromechanical impairments of diffuse axonal injury, Biomech. Model. Mechanobiol. 18 (2019) 361–374.
[11] A. Trotta, J.M. Clark, A. McGoldrick, M.D. Gilchrist, A.N. Annaidh, Biofidelic finite element modelling of brain trauma: importance of the scalp in simulating head impact, Int. J. Mech. Sci. 173 (2020) 105448.
[12] D. Espindola, S. Lee, G. Pinton, High frame-rate imaging and adaptive tracking of shear shock wave formation in the brain: a fullwave and experimental study, in: 2017 IEEE International Ultrasonics Symposium (IUS), 2017, pp. 1–4.
[13] D. Espíndola, S. Lee, G. Pinton, Shear shock waves observed in the brain, Phys. Rev. Appl. 8 (2017) 044024.
[14] D.I. Graham, J.H. Adams, J.A. Nicoll, W.L. Maxwell, T.A. Gennarelli, The nature, distribution and causes of traumatic brain injury, Brain Pathol. 5 (1995) 397–406.
[15] E.A. Zabolotskaya, M.F. Hamilton, Y.A. Ilinskii, G.D. Meegan, Modeling of nonlinear shear waves in soft solids, J. Acoust. Soc. Am. 116 (2004) 2807–2813.
[16] M. Destrade, E. Pucci, G. Saccomandi, Generalization of the Zabolotskaya equation to all incompressible isotropic elastic solids, Proc. R. Soc. A 475 (2019) 20190061.
[17] B.B. Tripathi, S. Chandrasekaran, G.F. Pinton, Super-resolved shear shock focusing in the human head, Brain Multiphys. 2 (2021) 100033.
[18] S. Chandrasekaran, F. Santibanez, B.B. Tripathi, R. DeRuiter, R.V. Bruegge, G. Pinton, In situ ultrasound imaging of shear shock waves in the porcine brain, J. Biomech. 134 (2022) 110913.
[19] M.T. Prange, S.S. Margulies, Regional, directional, and age-dependent properties of the brain undergoing large deformation, J. Biomech. Eng. 124 (2002) 244–252.
[20] S. Nicolle, M. Lounis, R. Willinger, Shear properties of brain tissue over a frequency range relevant for automotive impact situations: new experimental results, Stapp Car Crash J. 48 (2004) 389.
[21] A. Tamura, S. Hayashi, I. Watanabe, K. Nagayama, T. Matsumoto, Mechanical characterization of brain tissue in high-rate compression, J. Biomech. Sci. Eng. 2 (2007) 115–126.
[22] B. Rashid, M. Destrade, M.D. Gilchrist, Mechanical characterization of brain tissue in tension at dynamic strain rates, J. Mech. Behav. Biomed. Mater. 33 (2014) 43–54.
[23] J.D. Finan, S.N. Sundaresh, B.S. Elkin, I.I. G. M. McKhann, B. Morrison III, Regional mechanical properties of human brain tissue for computational models of traumatic brain injury, Acta Biomater. 55 (2017) 333–339.
[24] S. Budday, G. Sommer, G. Holzapfel, P. Steinmann, E. Kuhl, Viscoelastic parameter identification of human brain tissue, J. Mech. Behav. Biomed. Mater. 74 (2017) 463–476.
[25] L.V. Hiscox, M.D. McGarry, H. Schwarb, E.E.V. Houten, R.T. Pohlig, N. Roberts, G.R. Huesmann, A.Z. Burzynska, B.P. Sutton, C.H. Hillman, A.F. Kramer, N.J. Cohen, A.K. Barbey, K.D. Paulsen, C.L. Johnson, Standard-space atlas of the viscoelastic properties of the human brain, Hum. Brain Mapp. 41 (2020) 5282–5300.
[26] N.W. Tschoegl, Linear viscoelastic response, in: The Phenomenological Theory of Linear Viscoelastic Behavior: An Introduction, Springer, 1989, pp. 35–68.
[27] Y.C. Fung, Biomechanics: Mechanical Properties of Living Tissues, Springer, 1993.
[28] R. O'Connell, B. Budiansky, Measures of dissipation in viscoelastic media, Geophys. Res. Lett. 5 (1978) 5–8.
[29] S. Nicolle, M. Lounis, R. Willinger, J.F. Palierne, Shear linear behavior of brain tissue over a large frequency range, Biorheology 42 (2005) 209–223.
[30] Abaqus, Time domain viscoelasticity, 2022.
[31] K.R. Waters, M.S. Hughes, J. Mobley, G.H. Brandenburger, J.G. Miller, On the applicability of Kramers–Krönig relations for ultrasonic attenuation obeying a frequency power law, J. Acoust. Soc. Am. 108 (2000) 556–563.
[32] P. Moczo, J. Kristek, M. Gális, The Finite-Difference Modelling of Earthquake Motions: Waves and Ruptures, Cambridge University Press, 2014.
[33] B.B. Tripathi, D. Espíndola, G.F. Pinton, Piecewise parabolic method for propagation of shear shock waves in relaxing soft solids: one-dimensional case, Int. J. Numer. Method Biomed. Eng. 35 (2019) E3187.
[34] F. Mainardi, Fractional Calculus and Waves in Linear Viscoelasticity: An Introduction to Mathematical Models, World Scientific, 2010.
[35] L.V. Hiscox, C.L. Johnson, E. Barnhill, M.D. McGarry, J. Huston, E.J.V. Beek, J.M. Starr, N. Roberts, Magnetic resonance elastography (MRE) of the human brain: technique, findings and clinical applications, Phys. Med. Biol. 61 (2016) R401.
[36] G. Low, S.A. Kruse, D.J. Lomas, General review of magnetic resonance elastography, World J. Radiol. 8 (2016) 59.
[37] P. Kalra, B. Raterman, X. Mo, A. Kolipaka, Magnetic resonance elastography of brain: comparison between anisotropic and isotropic stiffness and its correlation to age, Magn. Reson. Med. 82 (2019) 671–679.
[38] D.P. Rosen, J. Jiang, A comparison of hyperelastic constitutive models applicable to shear wave elastography (SWE) data in tissue-mimicking materials, Phys. Med. Biol. 64 (2019) 055014.
[39] S. Budday, T.C. Ovaert, G.A. Holzapfel, P. Steinmann, E. Kuhl, Fifty shades of brain: a review on the mechanical testing and modeling of brain tissue, Arch. Comput. Methods Eng. 27 (2020) 1187–1230.
[40] B. Babaei, D. Fovargue, R.A. Lloyd, R. Miller, L. Jugé, M. Kaplan, R. Sinkus, D.A. Nordsletten, L.E. Bilston, Magnetic resonance elastography reconstruction for anisotropic tissues, Med. Image Anal. 74 (2021) 102212.
[41] L.E. Bilston, Soft tissue rheology and its implications for elastography: challenges and opportunities, NMR Biomed. 31 (2018) E3832.
[42] M.C. Murphy, J. Huston III, R.L. Ehman, MR elastography of the brain and its application in neurological diseases, Neuroimage 187 (2019) 176–183.
[43] A. Arani, M.C. Murphy, K.J. Glaser, A. Manduca, D.S. Lake, S.A. Kruse, C.R. Jack, R.L. Ehman, J. Huston, Measuring the effects of aging and sex on regional brain stiffness with MR elastography in healthy older adults, Neuroimage 111 (2015) 59–64.
[44] I. Sack, B. Beierbach, J. Wuerfel, D. Klatt, U. Hamhaber, S. Papazoglou, P. Martus, J. Braun, The impact of aging and gender on brain viscoelasticity, Neuroimage 46 (2009) 652–657.
[45] R. Vink, Large animal models of traumatic brain injury, J. Neurosci. Res. 96 (2018) 527–535.
[46] J.-X. Dai, Y.-B. Ma, N.-Y. Le, J. Cao, Y. Wang, Large animal models of traumatic brain injury, Int. J. Neurosci. 128 (2018) 243–254.
[47] S. Chatelin, A. Constantinesco, R. Willinger, Fifty years of brain tissue mechanical testing: from in vitro to in vivo investigations, Biorheology 47 (2010) 255–276.
[48] A. Gefen, S.S. Margulies, Are in vivo and in situ brain tissues mechanically similar? J. Biomech. 37 (2004) 1339–1352.
[49] B. Rashid, M. Destrade, M.D. Gilchrist, Temperature effects on brain tissue in compression, J. Mech. Behav. Biomed. Mater. 14 (2012) 113–118.
[50] Y.L. Liu, G.Y. Li, P. He, Z.Q. Mao, Y. Cao, Temperature-dependent elastic properties of brain tissues measured with the shear wave elastography method, J. Mech. Behav. Biomed. Mater. 65 (2017) 652–656.
[51] G. Peters, J. Meulman, A. Sauren, The applicability of the time/temperature superposition principle to brain tissue, Biorheology 34 (2017) 127–138.
[52] B. Rashid, M. Destrade, M.D. Gilchrist, Influence of preservation temperature on the measured mechanical properties of brain tissue, J. Biomech. 46 (2013) 1276–1281.
[53] A.E. Forte, S.M. Gentleman, D. Dini, On the characterization of the heterogeneous mechanical response of human brain tissue, Biomech. Model. Mechanobiol. 16 (2017) 907–920.
[54] J. Weickenmeier, M. Kurt, E. Ozkaya, R. de Rooij, T.C. Ovaert, R.L. Ehman, K.B. Pauly, E. Kuhl, Brain stiffens post mortem, J. Mech. Behav. Biomed. Mater. 84 (2018) 88–98.
[55] J.D. Finan, Biomechanical simulation of traumatic brain injury in the rat, Clin. Biomech. 64 (2019) 114–121.
[56] M. Hrapko, J.V. Dommelen, G. Peters, J. Wismans, The influence of test conditions on characterization of the mechanical properties of brain tissue, J. Biomech. Eng. 130 (2008) 031003.
[57] X. Li, Z. Zhou, S. Kleiven, An anatomically detailed and personalizable head injury model: significance of brain and white matter tract morphological variability on strain, Biomech. Model. Mechanobiol. 20 (2021) 403–431.
[58] C. Giordano, S. Kleiven, Connecting fractional anisotropy from medical images with mechanical anisotropy of a hyperviscoelastic fibre-reinforced constitutive model for brain tissue, J. R. Soc. Interface 11 (2014) 20130914.
[59] C. Giordano, S. Kleiven, Evaluation of axonal strain as a predictor for mild traumatic brain injuries using finite element modeling, Stapp Car Crash J. 58 (2014) 29–61.
[60] L.E. Miller, J.E. Urban, J.D. Stitzel, Development and validation of an atlas-based finite element brain model, Biomech. Model. Mechanobiol. 15 (2016) 1201–1214.
[61] Z. Cai, Y. Xia, Z. Bao, H. Mao, Creating a human head finite element model us-

ing a multi-block approach for predicting skull response and brain pressure, Comput Methods Biomech Biomed Engin 22 (2019) 169–179.
[62] Y. Chen, M. Ostoja-Starzewski, MRI-based finite element modeling of head trauma: spherically focusing shear waves, Acta Mech. 213 (2010) 155–167.
[63] T. Khanuja, H.N. Unni, Intracranial pressure–based validation and analysis of traumatic brain injury using a new three-dimensional finite element human head model, Proc. Inst. Mech. Eng. Part H J. Eng. Med. 234 (2020) 3–15.
[64] Z. Zhou, X. Li, S. Kleiven, Fluid–structure interaction simulation of the brain–skull interface for acute subdural haematoma prediction, Biomech. Model. Mechanobiol. 18 (2019) 155–173.
[65] E.G. Takhounts, R.H. Eppinger, J.Q. Campbell, R.E. Tannous, E.D. Power, L.S. Shook, On the development of the SIMon finite element head model, Stapp Car Crash J. 47 (2004) 385.
[66] E.G. Takhounts, S.A. Ridella, V. Hasija, R.E. Tannous, J.Q. Campbell, D. Malone, K. Danelson, J. Stitzel, S. Rowson, S. Duma, Investigation of traumatic brain injuries using the next generation of simulated injury monitor (SIMon) finite element head model, Stapp Car Crash J. 52 (2008) 403.
[67] D.R. Subramaniam, G. Unnikrishnan, A. Sundaramurthy, J.E. Rubio, V.B. Kote, J. Reifman, The importance of modeling the human cerebral vasculature in blunt trauma, Biomed. Eng. Online 20 (2021) 1–19.
[68] K.M. Tse, L.B. Tan, S.J. Lee, S.P. Lim, H.P. Lee, Development and validation of two subject-specific finite element models of human head against three cadaveric experiments, Int. J. Numer. Method Biomed. Eng. 30 (2014) 397–415.
[69] L. Zhang, K.H. Yang, R. Dwarampudi, K. Omori, T. Li, K. Chang, W.N. Hardy, T.B. Khalil, A.I. King, Recent advances in brain injury research: a new human head model development and validation, Stapp Car Crash J. 45 (2001) 375.
[70] B. Yang, K.-M. Tse, N. Chen, L.-B. Tan, Q.-Q. Zheng, H.-M. Yang, M. Hu, G. Pan, H.P. Lee, Development of a finite element head model for the study of impact head injury, Biomed. Res. Int. 2014 (2014).
[71] R. Willinger, H.-S. Kang, B. Diaw, Three-dimensional human head finite-element model validation against two experimental impacts, Ann. Biomed. Eng. 27 (1999) 403–410.
[72] R. Willinger, D. Baumgartner, Human head tolerance limits to specific injury mechanisms, Int. J. Crashworthiness 8 (2003) 605–617.
[73] R. Willinger, D. Baumgartner, Numerical and physical modelling of the human head under impact-towards new injury criteria, Int. J. Veh. Des. 32 (2003) 94–115.
[74] S. Ji, W. Zhao, J.C. Ford, J.G. Beckwith, R.P. Bolander, R.M. Greenwald, L.A. Flashman, K.D. Paulsen, T.W. McAllister, Group-wise evaluation and comparison of white matter fiber strain and maximum principal strain in sport-s-related concussion, J. Neurotrauma 32 (2015) 441–454.
[75] W. Zhao, S. Ji, Displacement and strain-based discrimination of head injury models across a wide range of blunt conditions, Ann. Biomed. Eng. 48 (2020) 1661–1677.
[76] W. Zhao, S. Ji, White matter anisotropy for impact simulation and response sampling in traumatic brain injury, J. Neurotrauma 36 (2019) 250–263.
[77] F.A. Fernandes, D. Tchepel, R.J.A. de Sousa, M. Ptak, Development and validation of a new finite element human head model: yet another head model (YEAHM), Eng. Comput. (Swansea) 35 (2018) 477–496.
[78] G. Migueis, F. Fernandes, M. Ptak, M. Ratajczak, R.A. de Sousa, Detection of bridging veins rupture and subdural haematoma onset using a finite element head model, Clin. Biomech. 63 (2019) 104–111.
[79] L. Shuck, S. Advani, Rheological response of human brain tissue in shear, J. Basic Eng. (1972) 905–911.
[80] S. Ji, H. Ghadyani, R.P. Bolander, J.G. Beckwith, J.C. Ford, T.W. McAllister, L.A. Flashman, K.D. Paulsen, K. Ernstrom, S. Jain, R. Raman, L. Zhang, R.M. Greenwald, Parametric comparisons of intracranial mechanical responses from three validated finite element models of the human head, Ann. Biomed. Eng. 42 (2014) 11–24.
[81] Z. Zhou, X. Li, Y. Liu, W.N. Hardy, S. Kleiven, Brain strain rate response: addressing computational ambiguity and experimental data for model validation, Brain Multiphys. (2023) 100073.
[82] D.B. MacManus, B. Pierrat, J.G. Murphy, M.D. Gilchrist, A viscoelastic analysis of the p56 mouse brain under large-deformation dynamic indentation, Acta Biomater. 48 (2017) 309–318.
[83] F. Eskandari, M. Shafieian, M.M. Aghdam, K. Laksari, Visco-hyperelastic properties of white and gray matters under tension: an ex-vivo study, in: The Annual International Conference of Iranian Society of Mechanical Engineers, 2020, p. 1584.
[84] S. Kleiven, Predictors for traumatic brain injuries evaluated through accident reconstructions, Stapp Car Crash J. 51 (2007) 81–114.
[85] T.B. Khalil, R.P. Hubbard, Parametric study of head response by finite element modeling, J. Biomech. 10 (1977) 119–132.
[86] D.B. MacManus, B. Pierrat, J.G. Murphy, M.D. Gilchrist, Region and species dependent mechanical properties of adolescent and young adult brain tissue, Sci. Rep. 7 (2017) 1–12.
[87] B. Rashid, M. Destrade, M.D. Gilchrist, Mechanical characterization of brain tissue in compression at dynamic strain rates, J. Mech. Behav. Biomed. Mater. 10 (2012) 23–38.
[88] R.J. Cloots, J.V. Dommelen, S. Kleiven, M. Geers, Multi-scale mechanics of traumatic brain injury: predicting axonal strains from head loads, Biomech. Model. Mechanobiol. 12 (2013) 137–150.
[89] L. Zhang, K.H. Yang, A.I. King, A proposed injury threshold for mild traumatic brain injury, J. Biomech. Eng. 126 (2004) 226–236.
[90] E.G. Takhounts, J.R. Crandall, K. Darvish, On the importance of nonlinearity of brain tissue under large deformations, Stapp Car Crash J. 47 (2003) 79.
[91] L. Zhang, K.H. Yang, A.I. King, Comparison of brain responses between frontal and lateral impacts by finite element modeling, J. Neurotrauma 18 (2001) 21–30.
[92] K. Mendis, R. Stalnaker, S. Advani, A constitutive relationship for large deformation finite element modeling of brain tissue, J. Biomech. Eng. 117 (1995) 279–285.
[93] M. Estes, J.H. McElhaney, Response of brain tissue to compressive loading, in: American Society of Mechanical Engineers Biomechanical and Human Factors Conference, 1970.
[94] X. Trosseille, C. Tarriere, F. Lavaste, F. Guillon, A. Domont, Development of a FEM of the human head according to a specific test protocol, in: 36st Stapp Car Crash Conference, 1992, p. 261.
[95] A.M. Nahum, R. Smith, C.C. Ward, Intracranial pressure dynamics during head impact, in: 21st Stapp Car Crash Conference, 1977, p. 073.
[96] X. Ning, Q. Zhu, Y. Lanir, S.S. Margulies, A transversely isotropic viscoelastic constitutive equation for brainstem undergoing finite deformation, J. Biomech. Eng. 128 (2006) 925–933.
[97] F. Eskandari, M. Shafieian, M.M. Aghdam, K. Laksari, Structural anisotropy vs. mechanical anisotropy: the contribution of axonal fibers to the material properties of brain white matter, Ann. Biomed. Eng. 49 (2021) 991–999.
[98] M. Hosseini-Farid, M. Ramzanpour, J. McLean, M. Ziejewski, G. Karami, A poro-hyper-viscoelastic rate-dependent constitutive modeling for the analysis of brain tissues, J. Mech. Behav. Biomed. Mater. 102 (2020) 103475.
[99] V. Libertiaux, F. Pascon, S. Cescotto, Experimental verification of brain tissue incompressibility using digital image correlation, J. Mech. Behav. Biomed. Mater. 4 (2011) 1177–1185.
[100] Y. Li, W. Zhang, Y.-C. Lu, C. Wu, Hyper-viscoelastic mechanical behavior of cranial pia mater in tension, Clin. Biomech. 80 (2020) 105108.
[101] L. Qian, H. Zhao, Y. Guo, Y. Li, M. Zhou, L. Yang, Z. Wang, Y. Sun, Influence of strain rate on indentation response of porcine brain, J. Mech. Behav. Biomed. Mater. 82 (2018) 210–217.
[102] M. Ramzanpour, M. Hosseini-Farid, J. McLean, M. Ziejewski, G. Karami, Visco-hyperelastic characterization of human brain white matter micro-level constituents in different strain rates, Med. Biol. Eng. Comput. 58 (2020) 2107–2118.
[103] N.L. Ramo, S.S. Shetye, F. Streijger, J.H. Lee, K.L. Troyer, B.K. Kwon, P. Cripton, C.M. Puttlitz, Comparison of in vivo and ex vivo viscoelastic behavior of the spinal cord, Acta Biomater. 68 (2018) 78–89.
[104] N.L. Ramo, K.L. Troyer, C.M. Puttlitz, Viscoelasticity of spinal cord and meningeal tissues, Acta Biomater. 75 (2018) 253–262.
[105] S.S. Shetye, K.L. Troyer, F. Streijger, J.H. Lee, B.K. Kwon, P.A. Cripton, C.M. Puttlitz, Nonlinear viscoelastic characterization of the porcine spinal cord, Acta Biomater. 10 (2014) 792–797.
[106] M. Shafieian, K.K. Darvish, J.R. Stone, Changes to the viscoelastic properties of brain tissue after traumatic axonal injury, J. Biomech. 42 (2009) 2136–2142.
[107] S. Qiu, W. Jiang, M.S. Alam, S. Chen, C. Lai, T. Wang, X. Li, J. Liu, M. Gao, Y. Tang, X. Li, J. Zeng, Y. Feng, Viscoelastic characterization of injured brain tissue after controlled cortical impact (CCI) using a mouse model, J. Neurosci. Methods 330 (2020) 108463.
[108] W. Li, D.E. Shepherd, D.M. Espino, Dynamic mechanical characterization and viscoelastic modeling of bovine brain tissue, J. Mech. Behav. Biomed. Mater. 114 (2021) 104204.
[109] S. Budday, G. Sommer, J. Haybaeck, P. Steinmann, G.A. Holzapfel, E. Kuhl, Rheological characterization of human brain tissue, Acta Biomater. 60 (2017) 315–329.
[110] S. Cheng, L.E. Bilston, Unconfined compression of white matter, J. Biomech. 40 (2007) 117–124.
[111] S.N. Sundaresh, J.D. Finan, B.S. Elkin, C. Lee, J. Xiao, B. Morrison III, Viscoelastic characterization of porcine brain tissue mechanical properties under indentation loading, Brain Multiphys. 2 (2021) 100041.
[112] B.S. Elkin, A.I. Ilankovan, B. Morrison III, A detailed viscoelastic characterization of the p17 and adult rat brain, J. Neurotrauma 28 (2011) 2235–2244.
[113] B.S. Elkin, B. Morrison, Viscoelastic properties of the p17 and adult rat brain from indentation in the coronal plane, J. Biomech. Eng. 135 (2013) 114507.
[114] J.D. Finan, B.S. Elkin, E.M. Pearson, I.L. Kalbian, B. Morrison, Viscoelastic properties of the rat brain in the sagittal plane: effects of anatomical structure and age, Ann. Biomed. Eng. 40 (2012) 70–78.
[115] J.D. Finan, E.M. Pearson, B. Morrison, Viscoelastic properties of the rat brain in the horizontal plane, in: Proceedings of the International Research Council on the Biomechanics of Injury Conference, Vol. 40, International Research Council on Biomechanics of Injury, 2012, pp. 474–485.
[116] S. MacLean, Brain tissue: analysis of mechanical properties, The Ohio State University, 2010 PhD thesis.
[117] M.A. Branch, T.F. Coleman, Y. Li, A subspace, interior, and conjugate gradient method for large-scale bound-constrained minimization problems, SIAM J. Sci. Comput. 21 (1999) 1–23.
[118] P. Virtanen, R. Gommers, T.E. Oliphant, M. Haberland, T. Reddy, D. Cournapeau, E. Burovski, P. Peterson, W. Weckesser, J. Bright, S.J. van der Walt, M. Brett, J. Wilson, K.J. Millman, N. Mayorov, A.R.J. Nelson, E. Jones, R. Kern, E. Larson, C.J. Carey, I. Polat, Y. Feng, E.W. Moore, J. VanderPlas, D. Laxalde, J. Perktold, R. Cimrman, I. Henriksen, E.A. Quintero, C.R. Harris, A.M. Archibald, A.H. Ribeiro, F. Pedregosa, P. van Mulbregt, A. Vijaykumar, A.P. Bardelli, A. Rothberg, A. Hilboll, A. Kloeckner, A. Scopatz, A. Lee, A. Rokem, C.N. Woods, C. Fulton, C. Masson, C. Haggstrom, C. Fitzgerald, D.A. Nicholson, D.R. Hagen, D.V. Pasechnik, E. Olivetti, E. Martin, E. Wieser, F. Silva, F. Lenders, F. Wilhelm, G. Young, G.A. Price, G.-L. Ingold, G.E. Allen,

G.R. Lee, H. Audren, I. Probst, J.P. Dietrich, J. Silterra, J.T. Webber, J. Slavic, J. Nothman, J. Buchner, J. Kulick, J.L. Schonberger, J.V. de Miranda Cardoso, J. Reimer, J. Harrington, J.L.C. Rodriguez, J. Nunez-Iglesias, J. Kuczynski, K. Tritz, M. Thoma, M. Newville, M. Kummerer, M. Bolingbroke, M. Tartre, M. Pak, N.J. Smith, N. Nowaczyk, N. Shebanov, O. Pavlyk, P.A. Brodtkorb, P. Lee, R.T. McGibbon, R. Feldbauer, S. Lewis, S. Tygier, S. Sievert, S. Vigna, S. Peterson, S. More, T. Pudlik, T. Oshima, T.J. Pingel, T.P. Robitaille, T. Spura, T.R. Jones, T. Cera, T. Leslie, T. Zito, T. Krauss, U. Upadhyay, Y.O. Halchenko, Y. Vazquez-Baeza, S. Contributors, SciPy 1.0: fundamental algorithms for scientific computing in python, Nat. Methods 17 (2020) 261–272.

[119] J.M. Carcione, Wave Fields in Real Media: Wave Propagation in Anisotropic, Anelastic, Porous and Electromagnetic Media, Elsevier, 2007.

[120] A. Mendizabal, I. Aguinaga, E. Sanchez, Characterisation and modelling of brain tissue for surgical simulation, J. Mech. Behav. Biomed. Mater. 45 (2015) 1–10.

[121] B. Rashid, M. Destrade, M.D. Gilchrist, Hyperelastic and viscoelastic properties of brain tissue in tension, in: ASME International Mechanical Engineering Congress and Exposition, Vol. 45189, American Society of Mechanical Engineers, 2012, pp. 921–929.

[122] H. Emmerich, M. Korn, Incorporation of attenuation into time-domain computations of seismic wave fields, Geophysics 52 (1987) 1252–1264.

[123] E. Blanc, D. Komatitsch, E. Chaljub, B. Lombard, Z. Xie, Highly accurate stability-preserving optimization of the Zener viscoelastic model, with application to wave propagation in the presence of strong attenuation, Geophys. J. Int. 205 (2016) 427–439.

[124] S. Holm, Models of linear viscoelasticity, in: Waves with Power-Law Attenuation, Springer, 2019, pp. 67–93.

[125] Y. Jiang, G. Li, L.-X. Qian, S. Liang, M. Destrade, Y. Cao, Measuring the linear and nonlinear elastic properties of brain tissue with shear waves and inverse analysis, Biomech. Model. Mechanobiol. 14 (2015) 1119–1128.

[126] B.S. Elkin, A. Ilankova, I. Morrison, Barclay, dynamic, regional mechanical properties of the porcine brain: indentation in the coronal plane, J. Biomech. Eng. 133 (2011) 071009.

[127] S. Budday, R. Nay, R. de Rooij, P. Steinmann, T. Wyrobek, T.C. Ovaert, E. Kuhl, Mechanical properties of gray and white matter brain tissue by indentation, J. Mech. Behav. Biomed. Mater. 46 (2015) 318–330.

[128] W. Zhang, R.-R. Zhang, F. Wu, L.-L. Feng, S.-B. Yu, C.W. Wu, Differences in the viscoelastic features of white and grey matter in tension, J. Biomech. 49 (2016) 3990–3995.

[129] D.B. MacManus, A. Menichetti, B. Depreitere, N. Famaey, J.V. Sloten, M. Gilchrist, Towards animal surrogates for characterising large strain dynamic mechanical properties of human brain tissue, Brain Multiphys. 1 (2020) 100018.

[130] A. Menichetti, D.B. MacManus, M.D. Gilchrist, B. Depreitere, J.V. Sloten, N. Famaey, Regional characterization of the dynamic mechanical properties of human brain tissue by microindentation, Int. J. Eng. Sci. 155 (2020) 103355.

[131] S.N. Sundaresh, J.D. Finan, B.S. Elkin, A.V. Basilio, G.M. McKhann, B. Morrison, Region-dependent viscoelastic properties of human brain tissue under large deformations, Ann. Biomed. Eng. (2022) 1–9.

[132] D.B. MacManus, B. Pierrat, J.G. Murphy, M.D. Gilchrist, Protection of cortex by overlying meninges tissue during dynamic indentation of the adolescent brain, Acta Biomater. 57 (2017) 384–394.

[133] C. Pan, F. Chen, J. Zhou, X. Li, F. Zhao, X. Zhang, Multiregional viscoelastic characterization of the corona radiata in the sagittal plane of the porcine brain, Med. Biol. Eng. Comput. 57 (2019) 615–622.

[134] C. Pan, Z. Huang, W. Wu, J. Zhou, X. Li, Multiregional viscoelastic properties of the porcine brain in the horizontal plane, Med. Biol. Eng. Comput. 60 (2022) 855–862.

[135] K. Miller, K. Chinzei, Constitutive modelling of brain tissue: experiment and theory, J. Biomech. 30 (1997) 1115–1121.

[136] K. Miller, Constitutive model of brain tissue suitable for finite element analysis of surgical procedures, J. Biomech. 32 (1999) 531–537.

[137] K. Miller, K. Chinzei, Mechanical properties of brain tissue in tension, J. Biomech. 35 (2002) 483–490.

[138] M.T. Prange, D.F. Meaney, S.S. Margulies, Defining brain mechanical properties: effects of region, direction, and species, Stapp Car Crash J. 44 (2000) 362.

[139] S. Jannesar, M. Allen, S. Mills, A. Gibbons, J.C. Bresnahan, E.A. Salegio, C.J. Sparrey, Compressive mechanical characterization of non-human primate spinal cord white matter, Acta Biomater. 74 (2018) 260–269.

[140] C.R. Bass, C.J. Planchak, R.S. Salzar, S.R. Lucas, K.A. Rafaels, B.S. Shender, G. Paskoff, The temperature-dependent viscoelasticity of porcine lumbar spine ligaments, Spine 32 (2007) E436–E442.

[141] K.L. Troyer, C.M. Puttlitz, Nonlinear viscoelasticty plays an essential role in the functional behavior of spinal ligaments, J. Biomech. 45 (2012) 684–691.

[142] K.L. Troyer, D.J. Estep, C.M. Puttlitz, Viscoelastic effects during loading play an integral role in soft tissue mechanics, Acta Biomater. 8 (2012) 234–243.

[143] Y. Chang, N. Kim, S. Stenfelt, The development of a whole-head human finite-element model for simulation of the transmission of bone-conducted sound, J. Acoust. Soc. Am. 140 (2016) 1635–1651.

[144] K.M. Tse, S.P. Lim, V.B.C. Tan, H.P. Lee, A review of head injury and finite element head models, Am. J. Eng. Technol. Soc. 1 (2014) 28–52.

[145] B. Rashid, M. Destrade, M.D. Gilchrist, Mechanical characterization of brain tissue in simple shear at dynamic strain rates, J. Mech. Behav. Biomed. Mater. 28 (2013) 71–85.

[146] B. Staber, J. Guilleminot, Stochastic modeling of a class of stored energy functions for incompressible hyperelastic materials with uncertainties, Comptes Rendus Mécanique 343 (2015) 503–514.

[147] B. Staber, J. Guilleminot, Stochastic modeling of the Ogden class of stored energy functions for hyperelastic materials: the compressible case, ZAMM J. Appl. Math. Mech. 97 (2017) 273–295.

[148] P. Chen, J. Guilleminot, Spatially-dependent material uncertainties in anisotropic nonlinear elasticity: stochastic modeling, identification, and propagation, Comput. Methods Appl. Mech. Eng. 394 (2022) 114897.

[149] S. Nolan, A. Smerzi, L. Pezzè, A machine learning approach to Bayesian parameter estimation, npj Quantum Inf. 7 (2021) 169.

[150] S.L. Brunton, J.L. Proctor, J.N. Kutz, Discovering governing equations from data by sparse identification of nonlinear dynamical systems, Proc. Natl. Acad. Sci. 113 (2016) 3932–3937.

[151] S.H. Rudy, S.L. Brunton, J.L. Proctor, J.N. Kutz, Data-driven discovery of partial differential equations, Sci. Adv. 3 (2017) E1602614.

[152] S.L. Brunton, J.N. Kutz, Data-Driven Science and Engineering: Machine Learning, Dynamical Systems, and Control, Cambridge University Press, 2019.

[153] S.L. Brunton, B.R. Noack, P. Koumoutsakos, Machine learning for fluid mechanics, Annu. Rev. Fluid Mech. 52 (2020) 477–508.

[154] M. Raissi, G.E. Karniadakis, Hidden physics models: machine learning of nonlinear partial differential equations, J. Comput. Phys. 357 (2018) 125–141.

[155] M. Raissi, P. Perdikaris, G.E. Karniadakis, Physics-informed neural networks: a deep learning framework for solving forward and inverse problems involving nonlinear partial differential equations, J. Comput. Phys. 378 (2019) 686–707.

[156] S. Cuomo, V.S.D. Cola, F. Giampaolo, G. Rozza, M. Raissi, F. Piccialli, Scientific machine learning through physics–informed neural networks: where we are and what's next, J. Sci. Comput. 92 (2022) 88.

[157] P. Benner, M. Ohlberger, A. Cohen, K. Willcox, Model Reduction and Approximation: Theory and Algorithms, SIAM, 2017.

[158] B. Peherstorfer, K. Willcox, Dynamic data-driven reduced-order models, Comput. Methods Appl. Mech. Eng. 291 (2015) 21–41.

[159] K. Lee, K.T. Carlberg, Model reduction of dynamical systems on nonlinear manifolds using deep convolutional autoencoders, J. Comput. Phys. 404 (2020) 108973.

[160] S. Fresca, A. Manzoni, POD-DL-ROM: Enhancing deep learning-based reduced order models for nonlinear parametrized PDEs by proper orthogonal decomposition, Comput. Methods Appl. Mech. Eng. 388 (2022) 114181.

[161] K. Bhattacharya, B. Hosseini, N.B. Kovachki, A.M. Stuart, Model reduction and neural networks for parametric PDEs, SMAI J. Comput. Math. 7 (2021) 121–157.

[162] M. Kast, M. Guo, J.S. Hesthaven, A non-intrusive multifidelity method for the reduced order modeling of nonlinear problems, Comput. Methods Appl. Mech. Eng. 364 (2020) 112947.

[163] J.S. Hesthaven, S. Ubbiali, Non-intrusive reduced order modeling of nonlinear problems using neural networks, J. Comput. Phys. 363 (2018) 55–78.

[164] M. Guo, A. Manzoni, M. Amendt, P. Conti, J.S. Hesthaven, Multi-fidelity regression using artificial neural networks: efficient approximation of parameter-dependent output quantities, Comput. Methods Appl. Mech. Eng. 389 (2022) 114378.

[165] L. Lu, P. Jin, G. Pang, Z. Zhang, G.E. Karniadakis, Learning nonlinear operators via DeepONet based on the universal approximation theorem of operators, Nat. Mach. Intell. 3 (2021) 218–229.

[166] L. Lu, R. Pestourie, S.G. Johnson, G. Romano, Multifidelity deep neural operators for efficient learning of partial differential equations with application to fast inverse design of nanoscale heat transport, Phys. Rev. Res. 4 (2022) 023210.

[167] S. Wang, H. Wang, P. Perdikaris, Improved architectures and training algorithms for deep operator networks, J. Sci. Comput. 92 (2022) 35.

[168] N.B. Kovachki, Machine learning and scientific computing, California Institute of Technology, 2022 PhD thesis.

[169] Z. Li, N. Kovachki, K. Azizzadenesheli, B. Liu, K. Bhattacharya, A. Stuart, A. Anandkumar, Fourier neural operator for parametric partial differential equations, in: International Conference on Learning Representations, 2021.

[170] N. Kovachki, Z. Li, B. Liu, K. Azizzadenesheli, K. Bhattacharya, A. Stuart, A. Anandkumar, Neural operator: learning maps between function spaces with applications to PDEs, J. Mach. Learn. Res. 24 (2023) 1–97.